



ORIGINAL RESEARCH ARTICLE

High-Temperature Oxidation and Hot Corrosion Behaviors and Mechanism of One Typical Aero-Engine Material 0Cr18Ni9 by One Novel Superhydrophobic and Oleophobic Ultrafine Dry Powder Extinguishing Agent

Yurong Liu, Rui Zhang, Hongling Jing, Daheng Yu, Renming Pan, and Ruiyu Chen

Submitted: 27 September 2023 / Revised: 30 October 2023 / Accepted: 10 November 2023

The macroscopic and microscopic surface morphology, products, kinetics, and reaction mechanism of one typical aero-engine material 0Cr18Ni9 in the cases of high-temperature oxidation and hot corrosion by a novel superhydrophobic and oleophobic ultrafine dry powder extinguishing agent (SHOU DPEA) are studied in a simulated aircraft engine compartment working environment. The results demonstrate that the oxidation and corrosion products both contain FeCr_2O_4 , Fe_2O_3 , and Fe_3O_4 . However, the presence of SHOU DPEA accelerates the corrosion within the alloy. The 0Cr18Ni9 substrate shows a L-shaped segregation phenomenon and a chromium-poor layer. Furthermore, the oxidation and corrosion kinetic curves of 0Cr18Ni9 are both parabolic. In particular, the high-temperature oxidation behavior of 0Cr18Ni9 can be divided into two stages: a rapid oxidation stage (0-96 hours) and an oxidation equilibrium stage (96-192 hours), and the hot corrosion process can be divided into two stages: an initial slow incubation stage from 0 to 48 hours, and an accelerated corrosion stage from 48 to 192 hours. Additionally, the chemical reaction mechanisms for oxidation/corrosion are illustrated.

Keywords 0Cr18Ni9, aviation firefighting, corrosion mechanism, high-temperature oxidation, superhydrophobic and oleophobic, ultra-fine dry powder extinguishing agent

1. Introduction

Fire protection is a crucial part of the operational safety of civil aircraft. Halon 1301, Halon 1211, and HFC-227ea are currently utilized as the fire extinguishing agents on civil aircraft. However, the Montreal Protocol on Substances that Deplete the Ozone Layer (Ref 1), signed in 1987, mandates that halon fire extinguishing agents should be phased out in non-essential configuration sites by 2010. Furthermore, the “Kigali Amendment”, ratified in 2016, calls for the gradual elimination of hydrofluorocarbons (HFCs) as fire extinguishing agents, including HFC-227ea, HFC-236fa, HFC-125, etc. (Ref 2). The International Civil Aviation Organization (ICAO) has mandated a ban on the use of Halon fire extinguishing agents in the

engine/APU compartments of civil aircraft for type certificate applications since December 31, 2014. Furthermore, the European Union Aviation Safety Agency (EASA) has proposed that the current Halon-type portable fire extinguishing agents should be withdrawn from use by December 31, 2025 (Ref 3). Consequently, the quest for innovative and suitable fire extinguishing agents for civil aircraft is an urgent issue that necessitates immediate attention.

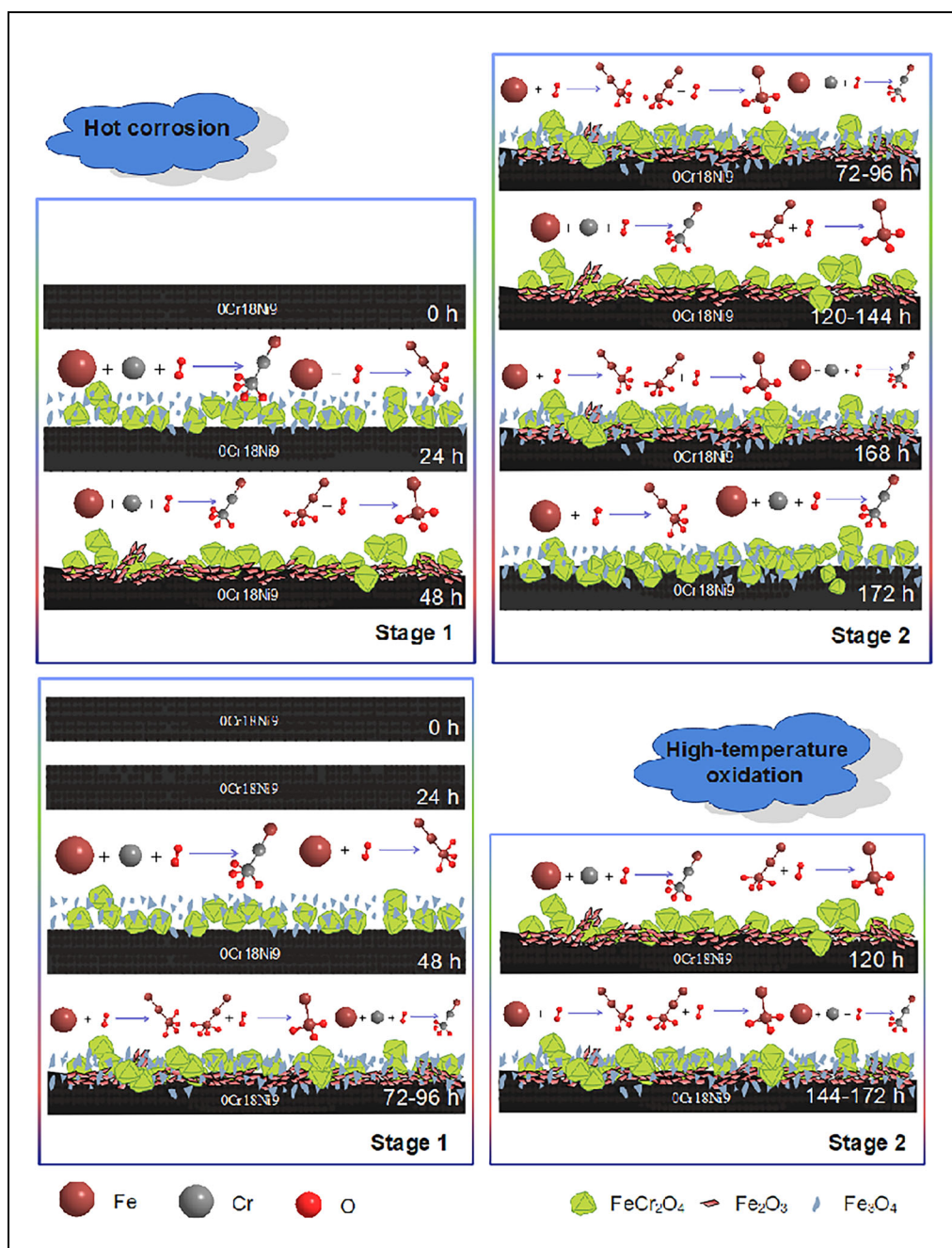
The Project entitled “The Evaluation of Alternative In-Flight Fire Suppressants for Full-scale Testing in Simulated Aircraft Engine Nacelles and Dry Bays,” conducted by the USA, demonstrated that ultra-fine dry powder extinguishing agents (UDPEAs) ($D_{90} < 20 \mu\text{m}$) exhibit low toxicity and environmental friendliness (Ref 4). UDPEAs have been found to possess approximately 2–5 times greater fire-extinguishing efficiency compared to Halon 1301 (Ref 5). Furthermore, UDPEAs exhibit gas-like characteristics and excellent full submergence capabilities (Ref 6) because of their small particle size and large specific surface area. Some innovative sodium bicarbonate UDPEA was proposed for use in the engine compartment of a combat vehicle (Ref 7). Xuan et al. (Ref 8) built the UDPEA ($D_{90} = 16.1 \mu\text{m}$) extinguishing system on a specific civil aircraft engine. They found that the UDPEA exhibited excellent spray performance and fire suppression capabilities, and it could be directly integrated into the existing fire suppression system pipe network of the aircraft. Therefore, UDPEAs have been evaluated as the most promising halon-alternative extinguishing agent for aircraft fire extinguishing systems (Ref 9-12).

It is worth noting that the current UDPEAs have some deficiencies such as high hygroscopicity, agglomeration tendency, and inadequate thermal stability. To address these issues,

Supplementary Information The online version contains supplementary material available at <https://doi.org/10.1007/s11665-023-08994-z>.

Yurong Liu, Renming Pan, and Ruiyu Chen, School of Chemistry and Chemical Engineering, Nanjing University of Science and Technology, Nanjing 210094 Jiangsu, People's Republic of China; and Rui Zhang, Hongling Jing, and Daheng Yu, Tianjin Aviation Electro-mechanical., Ltd, Tianjin 300300, People's Republic of China. Contact e-mails: panrenming@163.com and crynjust@njust.edu.cn.

Graphical Abstract



sodium bicarbonate UDPEA was modified using silicone oil and C6-fluorinated acrylate copolymer (FP) (Ref 13). The modified UDPEA was then processed into powder with the particle size distribution of D90 < 10 μm using an airflow pulverizer, generating a novel superhydrophobic and oleophobic ultra-fine dry powder extinguishing agent (SHOU DPEA). The SHOU DPEA possesses excellent thermal stability and demonstrates good dispersion properties. In addition, its superior hydrophobic and oleophobic characteristics significantly reduce the cleaning difficulty after the release of SHOU DPEA (Ref 14).

Aero engines frequently encounter harsh environments (Ref 15) characterized by high temperatures and corrosive media. Wang et al. (Ref 16) investigated the high-temperature

oxidation behaviors of 310S steel subjected to 800 $^{\circ}\text{C}$ for 170 hours and 500 hours. The results showed that the thickness of surface oxides increased with longer heat treatment durations. Zhang et al. (Ref 17) studied the evolution of oxide scales on austenitic stainless steel (SS) 304L at the temperatures of 600 $^{\circ}\text{C}$, 900 $^{\circ}\text{C}$, and 1250 $^{\circ}\text{C}$ with the heating periods of 30 minutes, 60 minutes, 90 minutes, and 120 minutes. Their research revealed that the surface of SS 304L underwent cyclic oxidation, generating fragmented structures. Zhou et al. (Ref 18) investigated the growth of oxidation scale on SS 304L plates in an industrial gas furnace at different temperatures and discovered that the formation of a protective film of Cr₂O₃ was primarily responsible for the oxidation resistance of SS 304L. Chen et al. (Ref 19) discovered that the corrosion rate of SS 304

in the marine atmosphere environment followed a power function law, with primary corrosion products being Fe_2O_3 , Fe_3O_4 , and FeOOH . I Saefuloh et al.(20) found that SS 304 experienced accelerated corrosion in acidic corrosive solutions as the temperature and concentration increased, primarily exhibiting uniform corrosion and localized pitting corrosion. Zhang et al. (Ref 21) found that SS 304 was vulnerable to pitting corrosion in aqueous sodium chloride solution, and the presence of Fe^{3+} accelerated the corrosion. Furthermore, it is worth noting that hot corrosion always worsens when damp particles containing sodium chloride enter the turbine engine. Jia et al. (Ref 22) demonstrated that molten salts, specifically sodium sulfate and sodium chloride, can significantly accelerated the oxidation of Nb-Si-based alloys at 900 °C, leading to catastrophic failure. The Ti2AlNb alloy exposed to a hot corrosion medium comprising a mixture of sodium chloride and sodium sulfate at temperatures of 923 K and 1023 K for 1000 hours exhibited increased hot corrosion with higher concentrations of sodium chloride in the salt medium (Ref 23).

It should be noted that the materials used in aero-engines may experience two corrosion cases after the application of SHOU DPEA as the fire extinguishing agent in the aircraft engine compartment: (1) Oxidation of aero-alloys at high temperatures. Even though previous research has studied the hot oxidation behavior of ordinary stainless steel (Ref 24, 25), there is still a need to address the corrosion products, mechanisms, and kinetics associated with this high-temperature oxidation process. (2) The hot corrosion of aero-alloy materials under the coupling effects of high temperature and SHOU DPEA or its decomposition products is fundamentally different from the previous studies. However, this work is essential and important for the substitution of halon extinguishing agents in civil aircraft fire extinguishing systems.

In the present study, the high-temperature oxidation and hot corrosion behaviors and mechanism of one typical aero-engine material 0Cr18Ni9 (Ref 26, 27) (known as SS 304 in the American standard) by a novel SHOU DPEA are studied in a simulated aircraft engine compartment working environment. The evolution of oxidation or corrosion was observed via a high definition camera, metallographic microscope and scanning electron microscope (SEM). Characterization of the corrosion products was conducted using techniques such as energy dispersive spectrometer (EDS), Fourier transform infrared spectroscopy (FTIR), and x-ray diffraction (XRD). Corrosion kinetics was used to evaluate the rate of oxidation or corrosion. The oxidation and corrosion mechanisms were investigated to provide a scientific basis for the development of safer and more environmentally friendly aircraft fire suppression systems. Additionally, this research also offers valuable insights for researchers in the field of aerospace engineering regarding material performance and corrosion behavior when using UDPEA as a fire extinguishing agent.

2. Experimental and Theoretical Background

2.1 Materials

The novel SHOU DPEA (Ref 14) with the particle size of $D_{90} = 6.1 \mu\text{m}$ was used in this study. The necessary materials for formulating the fire extinguishing powder, including sodium bicarbonate, mica, talcum, activated clay, zeolite, nano calcium

Table 1 Chemical compositions of 0Cr18Ni9 alloy steel (wt.%) (Ref 28)

C	Si	Mn	S	Cr	Ni	P	Fe
0.07	0.41	1.76	0.001	18	8.85	0.019	Bal

carbonate, and silicone oil, were provided by Aladdin Co., Ltd. Active clay (1.35%), nano calcium carbonate (1.35%), zeolite (1.9%), mica (2.7%), talc (2.7%), and sodium bicarbonate (90%) were proportionately combined and modified by silicone oil and FP (Ref 13). The specified powder was subsequently air-crushed to achieve the particle size of $D_{90} < 10 \mu\text{m}$. The chemical composition of 0Cr18Ni9 is presented in Table 1, and the function of auxiliary ingredient of SHOU DPEA is shown in Table S1 in the Supplementary Materials.

2.2 Experimental Procedure

Standard samples of the 0Cr18Ni9 alloy, with dimensions of 10 mm × 10 mm × 1.5 mm, were prepared and polished to obtain a mirror-like surface. Figure 1 depicts the surface morphology of 0Cr18Ni9 under metallographic microscope. A smooth surface facilitates better control over variables, minimizes the interference from alloy defects, and enables an exploration of the oxidation/corrosion mechanisms of stainless steel when exposed to high temperatures and SHOU DPEA. Acetone, methyl propymethone, and solvent oil (from Aladdin Co., Ltd.) were used to clean the surface of the sample by ultrasound. Afterwards, the samples were dried for one hour at 60 °C. Three samples were placed in a ceramic crucible for high-temperature oxidation tests. In order to simulate the 0Cr18Ni9 alloy exposed to SHOU DPEA inside an aircraft engine compartment, additional three 0Cr18Ni9 alloy samples were placed in the ceramic crucible with SHOU DPEA. The upper surface of each 0Cr18Ni9 alloy sample was coated with SHOU DPEA for the hot corrosion tests. Then, two crucibles containing the samples were placed inside the tube furnace (from Hefei Kejing Material Technology Co., Ltd.). The temperature was raised from room temperature to 871 °C at the heating rate of 10 °C/min. It was sustained at 871 °C for 10 hours before allowing the samples to cool naturally. Dry air with the flow rate of 100 mL/min was continuously introduced into the tube furnace, while the pressure was maintained at the standard atmospheric level. A schematic diagram illustrates the corrosion of the 0Cr18Ni9 alloy by SHOU DPEA in the engine compartment of the model airplane, as presented in Fig. 2. Figure 3 displays the time-dependent change in operating temperature within the simulated aircraft engine compartment, following a 24-hour cycle period. The tests involve a total of eight cycles. The mass changes of the 0Cr18Ni9 alloy samples were measured every 24 hours throughout the 192-hour duration of high-temperature oxidation and hot corrosion tests, using an electronic scale (Tsushima) with a precision of 10^{-5} g. Each piece was weighed at least five times to calculate its average weight.

2.3 Characterization

The macroscopic morphology of the 0Cr18Ni9 alloy samples was captured using a high-definition camera. The

SEM (JSM-IT500HR) and a long working distance metallographic microscope (PS888L) with the magnification of 100 were used to examine the surface flaws and micro-morphology of the samples, respectively. The elemental composition of the sample surfaces was determined using EDS. FTIR (Bruker INVENIO) was used to identify the functional groups of the corrosion products, and the XRD (Rikaku Rigaku D/max-2500pc) was used to determine the structure of the corrosion products.

2.4 Theoretical Background

The theory of oxide film growth postulates that oxygen ions diffuse through the anionic vacancies within the film and traverse the oxide film to reach the metal surface. Simultaneously, electrons move outward from the metal surface, promoting the growth of the oxide film at the interface between the metal and the oxide film. The equilibrium velocity of oxygen ions and electrons or the displacement rate of anionic vacancies

within the oxide film serves as controlling factors for the corrosion rate. Actual alloys consist of multiple grains with intergranular pores. The chemical process initiates with the formation of a solid phase when the gas diffuses into the particles and reaches the grain surface.

Oxygen undergoes diffusion towards the O_2/MO interface in the high-temperature atmosphere, and the reactions are presented as follows:



Figure 4 illustrates the reactions at the phase boundary and the processes of particle transport during the metal oxidation process, where positive and negative ions diffuse through the oxide coating.

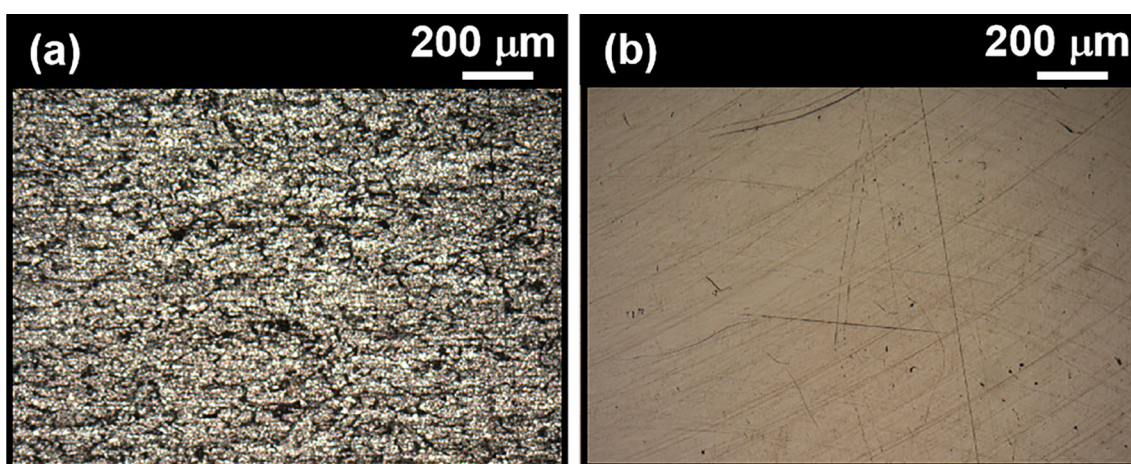


Fig. 1 0Cr18Ni9 surface morphology (a) before and (b) after polishing

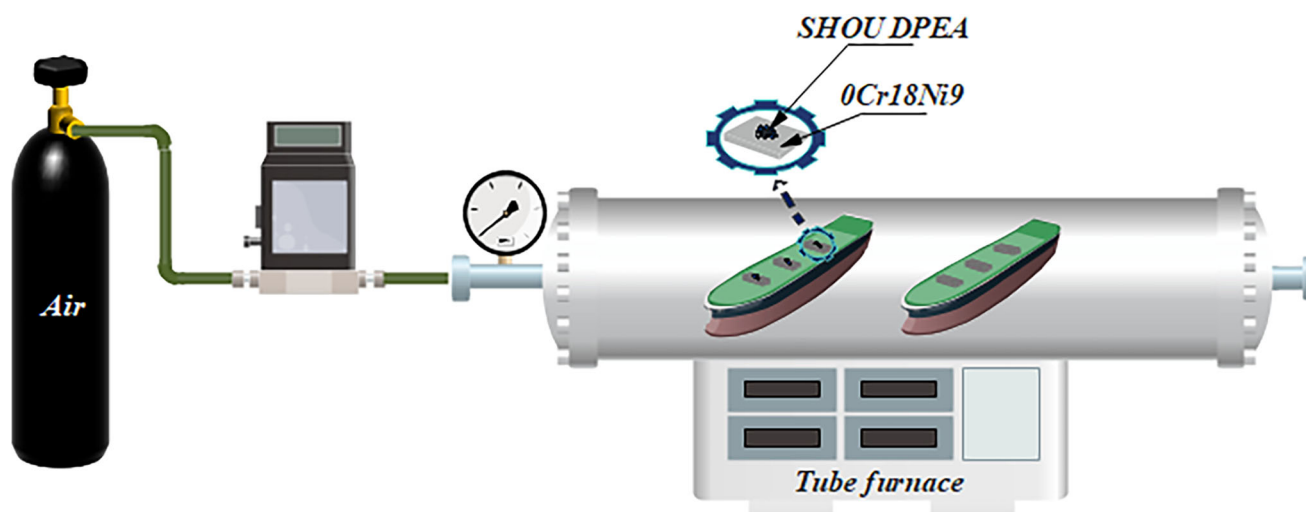


Fig. 2 Simulation of corrosion of 0Cr18Ni9 alloy by SHOU DPEA in the working environment of aircraft engine compartment

Wagner's parabolic law (29) is applicable to the weight gain method (30), which measures the corrosion rate resulting from oxidation over time at high temperatures. The oxidation process of metals is controlled by the diffusion of positive and negative ions within the oxide film, described by Eq. 4 (Ref 31, 32):

$$\left(\frac{\Delta W}{A}\right)^n = K_n t + C \quad (\text{Eq 4})$$

where ΔW , A , n , t , and K_n represent the oxidative weight gain (mg/cm^2), the area of oxidation (cm^2), the non-dimensional reaction index, the time (h), and the reaction rate coefficient (mg/h), respectively.

Equation 5 is obtained by taking the logarithm of Eq. 4:

$$\ln\left(\frac{\Delta W}{A}\right) = \frac{1}{n} \ln K_n + \frac{1}{n} \ln t \quad (\text{Eq 5})$$

3. Results and Discussions

3.1 Macroscopic Morphology Analysis

3.1.1 High-Temperature Oxidation. The macroscopic surface morphology of 0Cr18Ni9 during different high-temperature oxidation cycles is presented in Fig. 5. At 24 hours (Fig. 5b), the alloy surface appeared flat, characterized by a lighter central section and darker hues towards the edges. The

surface of alloy exhibited predominantly gray and black at 48 hours (Fig. 5c). Diamond-shaped pits were observed in Fig. 5(d). By 96 hours (Fig. 5e), the first layer of the surface was stripped, revealing a dark brown center and a light gray margin. Subsequently, numerous circular holes formed on the surface of alloy at 120 hours (Fig. 5f). As the oxidation time increased, these holes became more prominent and formed a circular pattern, as shown in Fig. 5(g). No noticeable radial oxidation trend was observed on the alloy surface after 144 hours, as shown in Fig. 5(h) and (i).

3.1.2 Hot Corrosion. The macroscopic surface morphology of 0Cr18Ni9 during different corrosion cycles is depicted in Fig. 6. On the surface of the alloy, a white crystalline

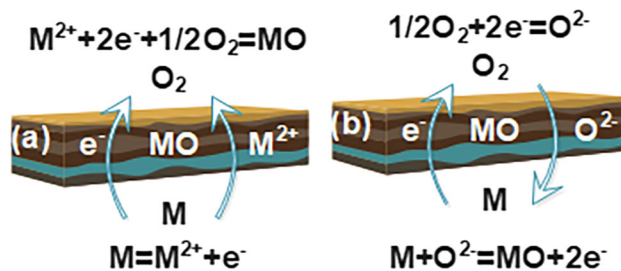


Fig. 4 Phase boundary reactions and particle transport processes in the metal oxidation. (a) cation motion, (b) anion motion

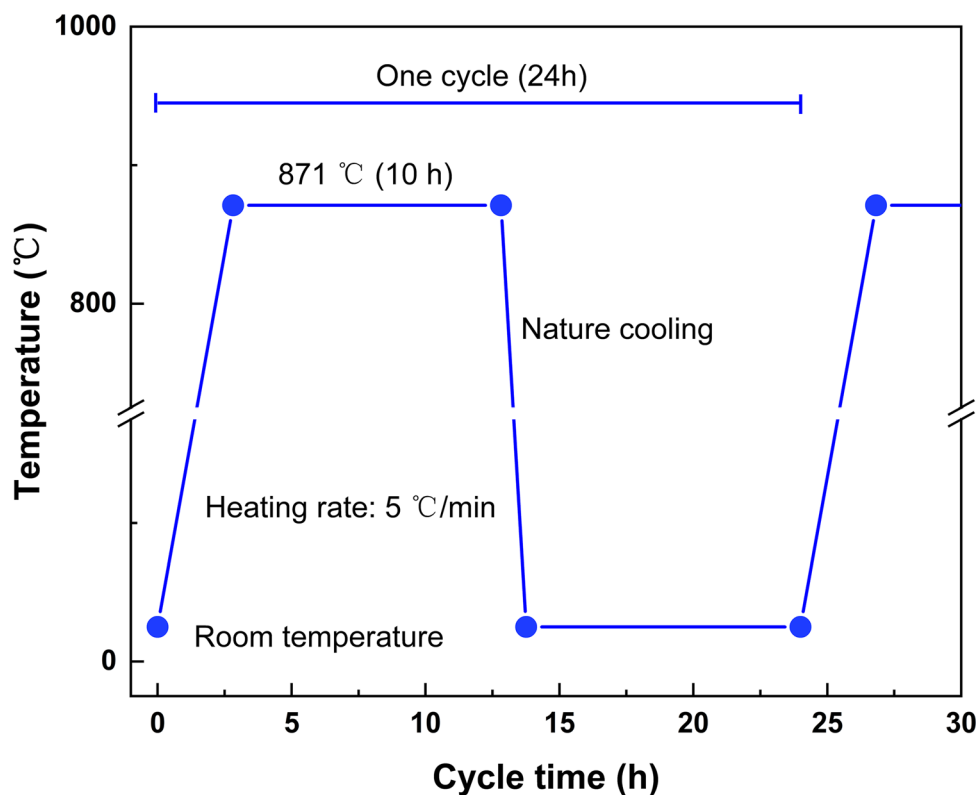


Fig. 3 Simulation of aircraft engine compartment operating temperatures over time

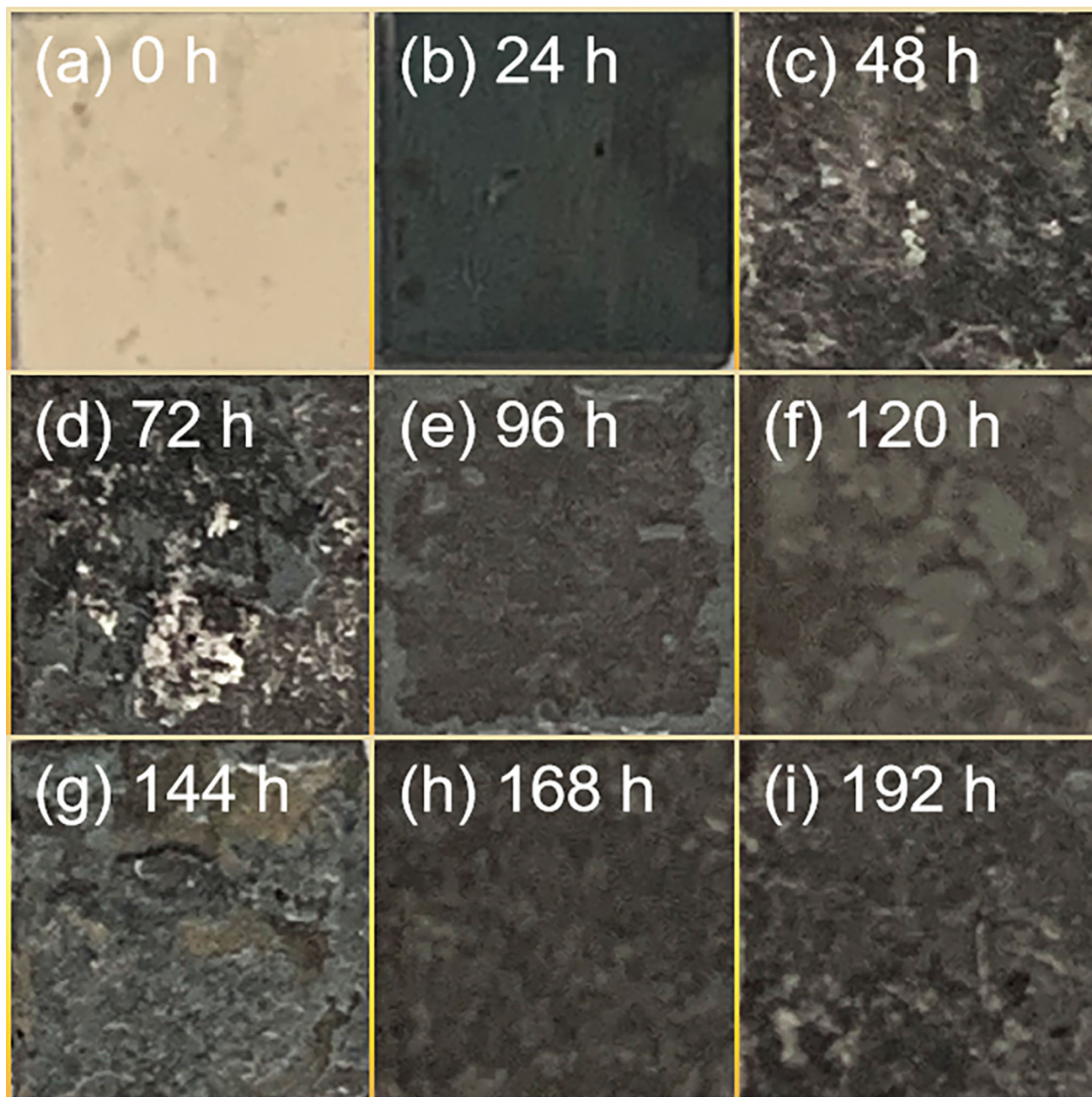


Fig. 5 Macroscopic surface topography of 0Cr18Ni9 during different high-temperature oxidation cycles

material and an L-shaped segregation phenomenon (Ref 33) could be observed at 24 hours. The white crystalline material could potentially be sodium carbonate crystals formed as a result of the pyrolysis of SHOU DPEA. By 48 hours, the corrosion intensified, leading to the spalling off of the block-like iron oxide in the center region (Fig. 6c). The surface of the alloy exhibited a dark yellow color, possibly indicating the occurrence of yellow-hued sodium flame reaction. The corrosion pits extended into the surrounding area as the corrosion cycle progressed, resulting in the increased corrosion areas and noticeable color differences on the surface, as illustrated in Fig. 6(d). At 96 hours, the initial surface layer was essentially peeled off, as shown in Fig. 6(e), revealing a circular depression. At 120 hours (Fig. 6f), severe cracking was

observed on the alloy surface, which appeared dark red, possibly due to the rust formation. Sub-triangular corrosion pits (Fig. 6g) reappeared at 144 hours, with a brown pit interior and a yellowish-gray pit exterior. The surface of the alloy showed island-like porous clusters at 168 hours, as depicted in Fig. 6h (Ref 34). Subsequently, raised areas on the alloy surface peeled off again, with patches appearing in dark red and yellowish-gray hues throughout the alloy surface.

3.1.3 Comparison. Figure 7 depicts the comparison of the macroscopic morphology of 0Cr18Ni9 at 24 hours, 96 hours, and 192 hours for the cases of hot corrosion and high-temperature oxidation. The surface of the 0Cr18Ni9 alloy, which was oxidized at 871 °C, appeared flat at 24 hours (Fig. 7b). However, the surface segregation phenomenon was

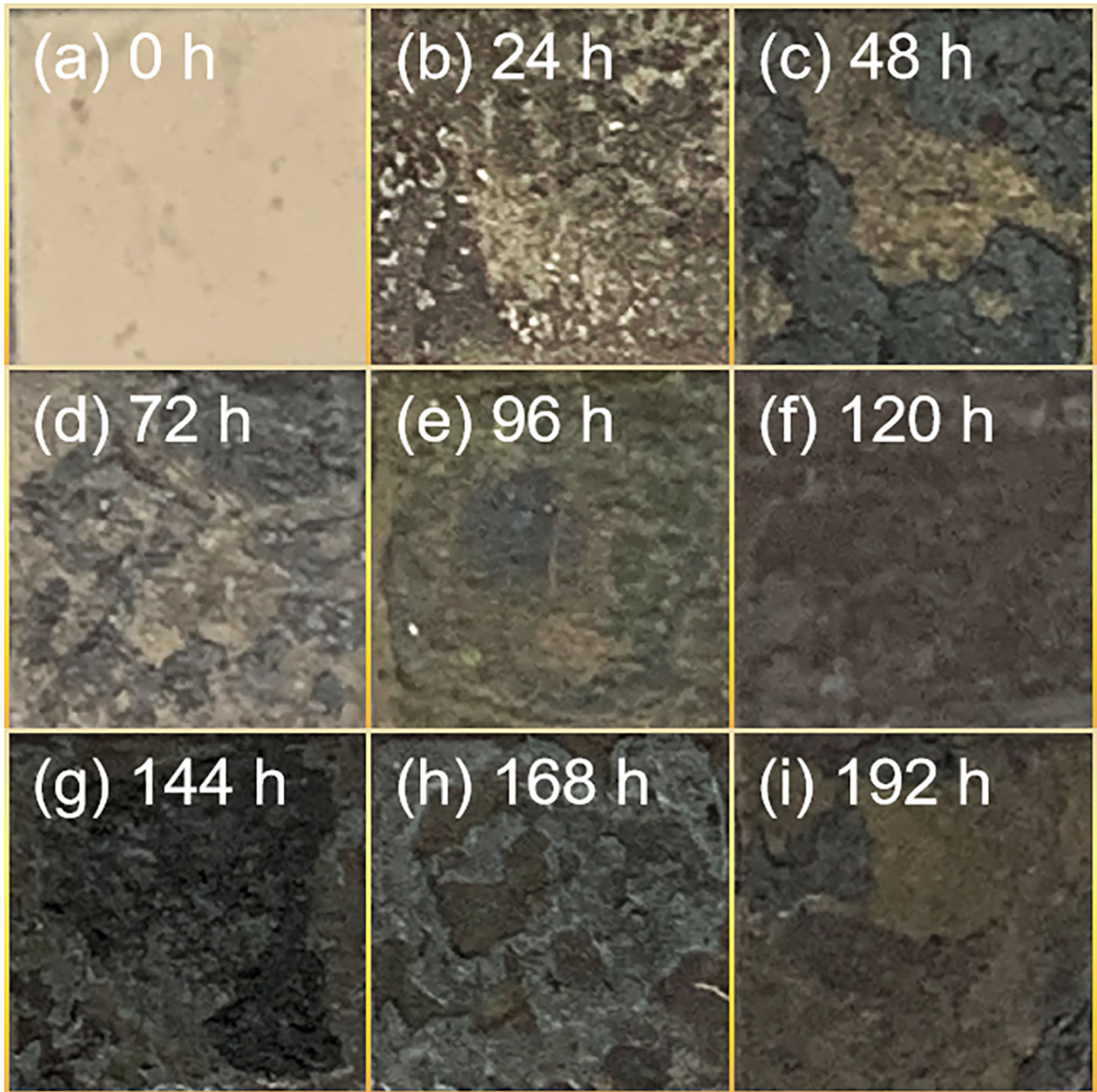


Fig. 6 Macroscopic surface topography of 0Cr18Ni9 during different hot corrosion cycles

evident when the SHOU DPEA was present, as shown in Fig. 7(a). The atoms within the 0Cr18Ni9 alloy material were redistributed along the grain boundaries on the surface and within the alloy under prolonged high-temperature conditions. This resulted in a significantly higher concentration of solutes or impurities at the interface in comparison to the interior of the alloy. Interestingly, the surface morphology of the 0Cr18Ni9 alloy remained similar at 96 hours for the cases of hot corrosion and high-temperature oxidation, as depicted in Fig. 7(c) and (d). However, when exposed to a molten salt medium containing SHOU DPEA, the surface of 0Cr18Ni9 exhibited a dark yellow color. By 192 hours, the oxidation process of the 0Cr18Ni9 reaches a relatively stable state, with no apparent ongoing oxidation or increasing trend in the formation of oxide

products (Fig. 7f, 5), while the corrosion continued (Fig. 6), leading to the formation of steps on the surface in Fig. 7(e). These observations suggest that the alloy's surface has achieved a state of equilibrium in terms of its oxidation behavior, suggesting that the formed oxide layer provides effective protection against continued oxidation, however, the SHOU DPEA accelerated the corrosion of 0Cr18Ni9 at high temperatures.

3.2 Micromorphology Analysis

3.2.1 High-Temperature Oxidation. The microscopic morphology of 0Cr18Ni9 during high-temperature oxidation over time is depicted in Fig. 8. A slight triangular contour

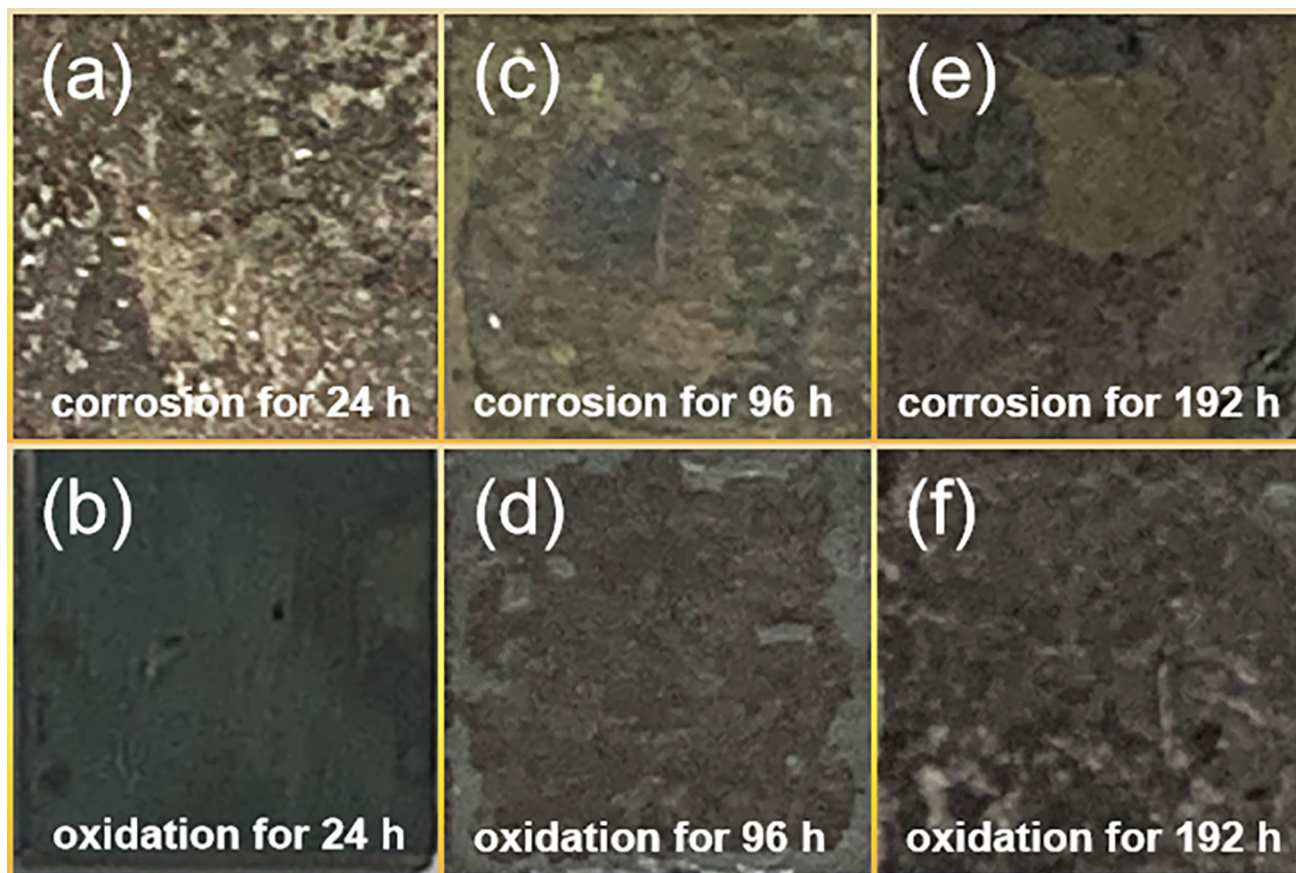


Fig. 7 Macroscopic topography of 0Cr18Ni9 at 24, 96, and 192 hours for high-temperature oxidation and hot corrosion

formed on the surface of the substrate in the first oxidation cycle, as shown in Fig. 8(b). At high temperatures, the formation of ferrite, a crystalline phase in stainless steel, can occur. The formation of ferrite is influenced by the alloy's chemical composition and temperature. During high-temperature oxidation of stainless steel, the formation of ferrite can lead to the appearance of triangular contours on the alloy's surface. Significant triangular pits, which are similar to those presented in Fig. 8(c) and 9(b), began to form on the surface of the substrate at 48 hours. These pits were primarily caused by the formation of ferrite. After oxidation for 72 hours (Fig. 8d), continuous dense boundary appeared on the surface of the alloy. These bands were characterized by densely packed oxidation products on one side and a porous structure on the other side. In Fig. 8e, the thick oxide layer ruptured after the fourth oxidation cycle, resulting in the formation of small sub-circular particles on the surface and tiny pores within the intact oxide layer. The above phenomenon mainly originated from the formation of ferrite. The alloy gradually transformed from ferrite to austenite, with ferrite nucleation and growth occurring simultaneously. Upon cooling, the untransformed ferrite that failed to convert into austenite continued to remain within the alloy, leading to a tendency for central segregation (Ref 35). Triangular craters reappeared at the end of the fifth oxidation cycle and continued to develop in a longitudinal orientation, as shown in Fig. 8(f). Figure 8(g) showed little spalling at the fissures, and the porous structure corresponded to spinel, which is likely to be Fe-Cr oxide (Ref 30). The corrosion extended to

depth along the longitudinal direction, as shown in Fig. 8(h), forming four steps where the dense needle-like structure may be Fe_2O_3 (Ref 34). At 192 hours, a granular exfoliation appeared on the surface of substrate.

3.2.2 Hot Corrosion. The microscopic surface morphology of 0Cr18Ni9 during hot corrosion over time is illustrated in Fig. 9. Figure 9a represents the initial smooth morphology of 0Cr18Ni9 before corrosion. As shown in Fig. 9(b), corrosion products on the surface of sample began to nucleate and expand, resulting in the formation of gaps. This phenomenon primarily occurred at high temperatures when molten salt provided a stable ionic electrolyte that deposited onto the surface of the alloy. This deposition facilitates a reaction between the ions in the molten salt and the metal ions, promoting the dissolution of the metal. The corrosion products may consist of loose iron oxides, which failed to prevent the penetration of oxygen from the molten salt of SHOU DPEA into the stainless steel matrix. After corrosion for 48 hours, the surface morphology of the substrate tended to become organized, forming cluster rosettes as shown in Fig. 9(c). Cross fractures appeared on the surface during the third corrosion cycle, and the rosette-shaped corrosion products became smaller and finer, as illustrated in Fig. 9(d). Additionally, clear cracking of the corrosion product was observed at the one-micron scale. Notably, the surface morphology of the substrate became organized again, with scattered rosette-shaped corrosion products in Fig. 9(e). With the increase in corrosion time, as shown in Fig. 9(f), the surface of the sample exhibited

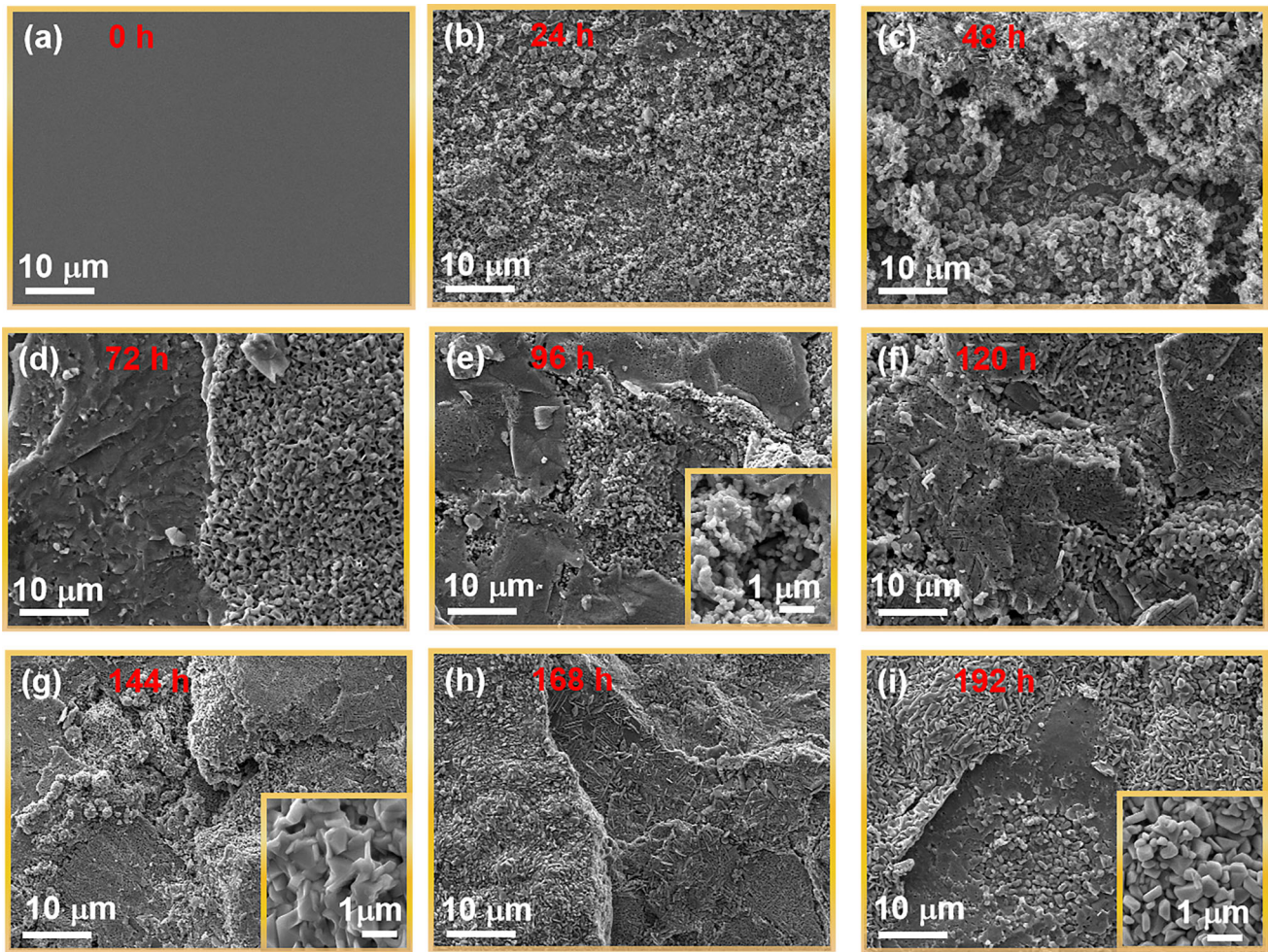


Fig. 8 Microscopic morphology of 0Cr18Ni9 during high-temperature oxidation over time

noticeable depressions, and cracks containing material with a spinel structure, which could potentially be Fe-Cr oxides. Interestingly, a microscopic morphology resembling the Danxia landscape was observed in 0Cr18Ni9, where 'hills' were grouped together, characterized by steep cliff slopes in an orderly form, resembling the natural formation of mountains (Fig. 9g). After 168 hours of corrosion, exfoliated columnar spinel appeared on the surface, resembling the natural landslide morphology (Fig. 9h). The square, mountain-like morphology in Fig. 9(h) was similar to that in Fig. 9(g). Meanwhile, the corrosion products exhibited an angular shape, and the cracks resembled hornet's nests, possibly due to the carbon dioxide released from the pyrolysis of SHOU DPEA within the alloy.

3.2.3 Comparison. Figure 10 illustrates the microscopic morphology of 0Cr18Ni9 at 24 hours, 96 hours, and 192 hours in the cases of high-temperature oxidation and hot corrosion. Following the initial cycle, the surface of the oxidized 0Cr18Ni9 alloy exhibited a snowflake-like pattern, with faint triangular traces visible in the central area (Fig. 10b). Conversely, triangular holes appeared on the surface of alloy after hot corrosion, as shown in Fig. 10(a). The adhesion of corrosion products to the alloy was notably weak (Ref 36), allowing the SHOU DPEA to easily penetrate the inner part of the alloy and accelerate corrosion through these holes. Subsequently, at the end of the fourth cycle, partial ruptures emerged

on the surface of the oxidized alloy, forming round and small granular ruptures (Fig. 10d). In contrast, the corroded sample exhibited a rosette pattern on its surface (Fig. 10c), indicating a tendency towards complete corrosion. By the end of the final cycle, no inclination towards further oxidation was observed on the surface of the oxidized alloy Fig. 10f). However, the surface of the corroded alloy exhibited a square, mountainous morphology with a flat top and steep sides (Fig. 10e). The cracks closely resembled hornets' nests in shape and provided perfect access for oxygen, consequently accelerating the corrosion of the non-protective substrate.

3.3 Chemical Elements Analysis

3.3.1 High-Temperature Oxidation. The variations in elemental content of 0Cr18Ni9 during high-temperature oxidation as a function of time are shown in Fig. 11. Our measurements revealed that the oxygen content was the highest, indicating that the alloying elements in 0Cr18Ni9 had diffused to the surface of the substrate and reacted with oxygen. After 144 hours, the oxygen content had significantly increased, resulting in iron-to-oxygen ratios ranging between 0.26 and 0.31. It was worth noting that common iron oxides typically exhibit iron-to-oxygen ratios falling within the range of 0.66 to 1 (with ferric oxide, tetra ferric oxide, and ferrous oxide

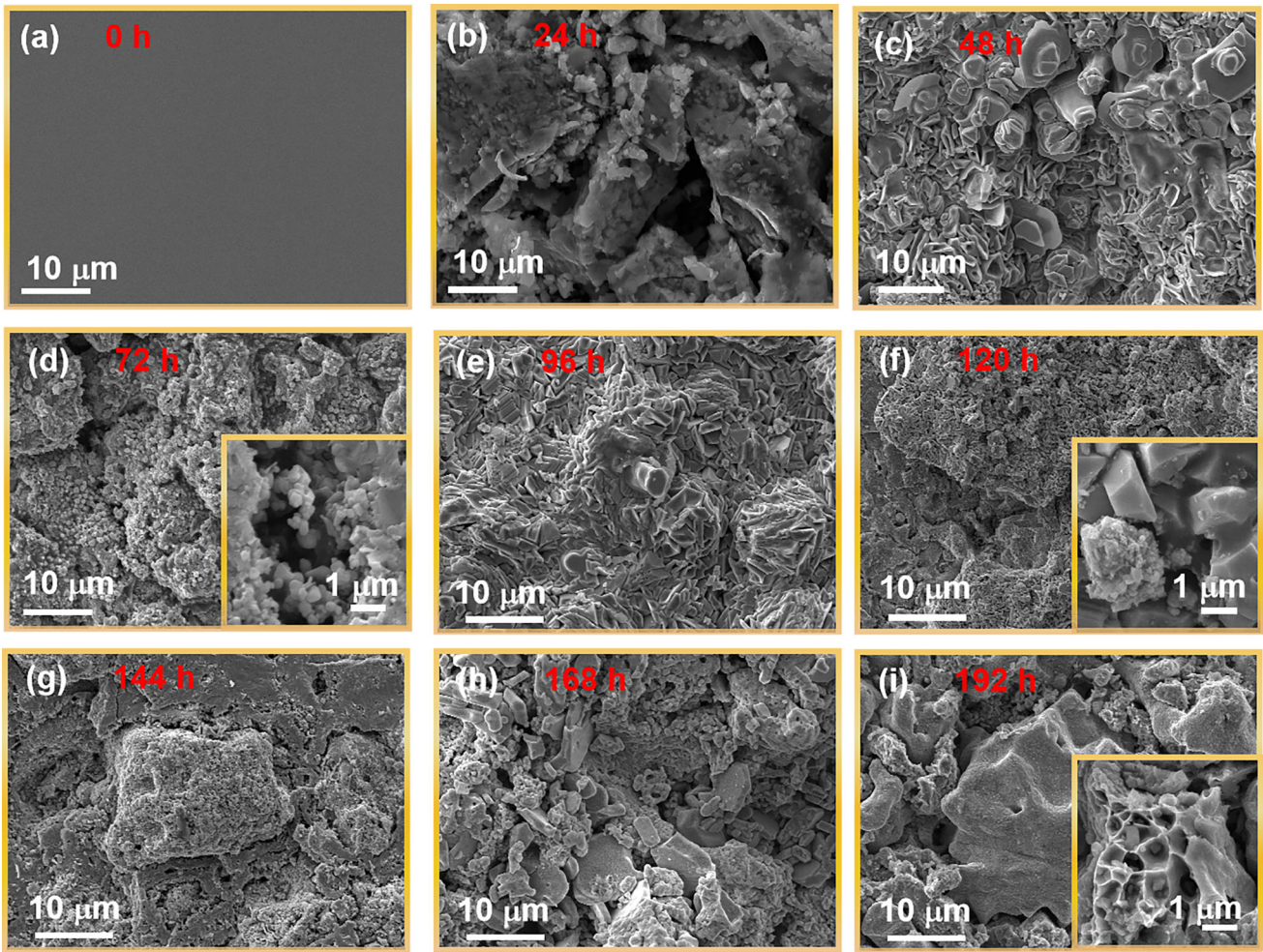


Fig. 9 Microscopic morphology of 0Cr18Ni9 during hot corrosion over time

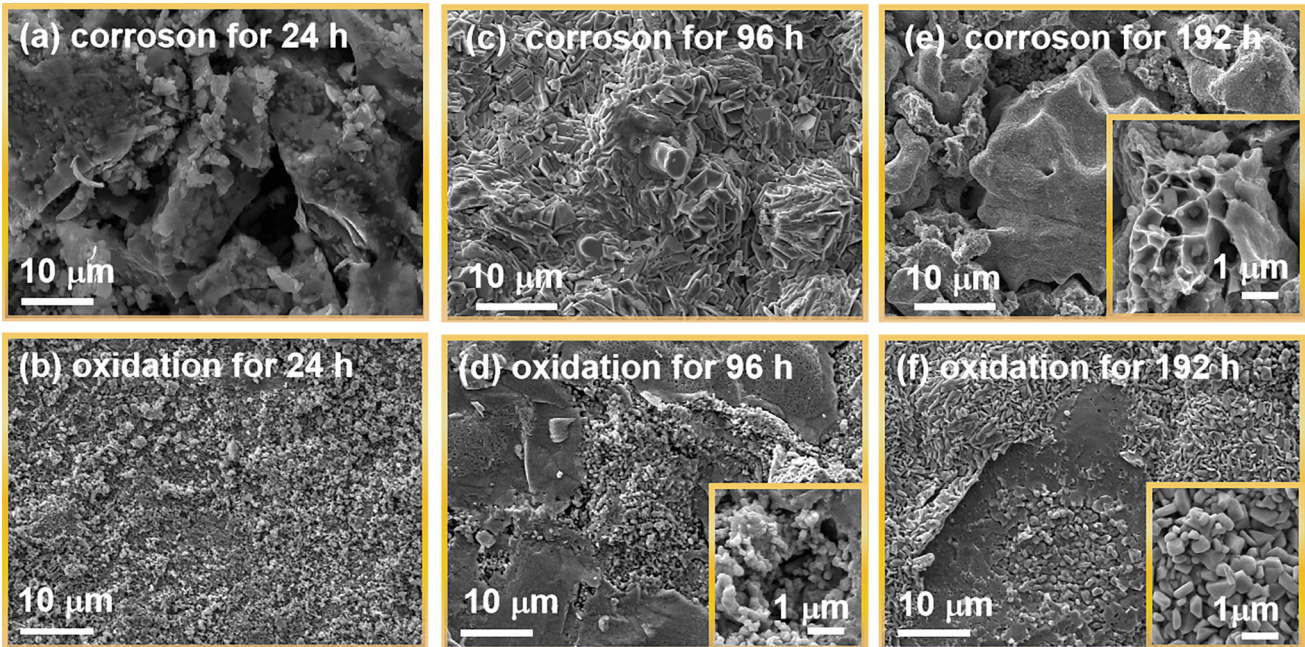


Fig. 10 Microtopography of 0Cr18Ni9 at 24, 96, and 192 hours for high-temperature oxidation and hot corrosion

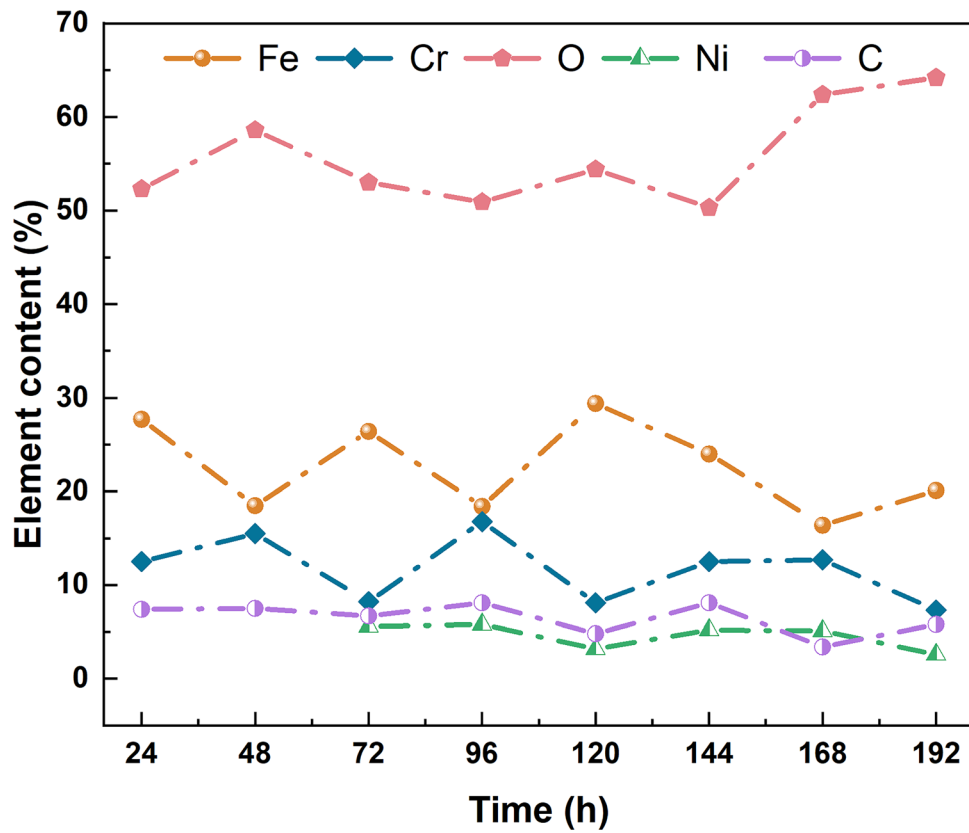


Fig. 11 Element content of 0Cr18Ni9 during high-temperature oxidation as a function of time

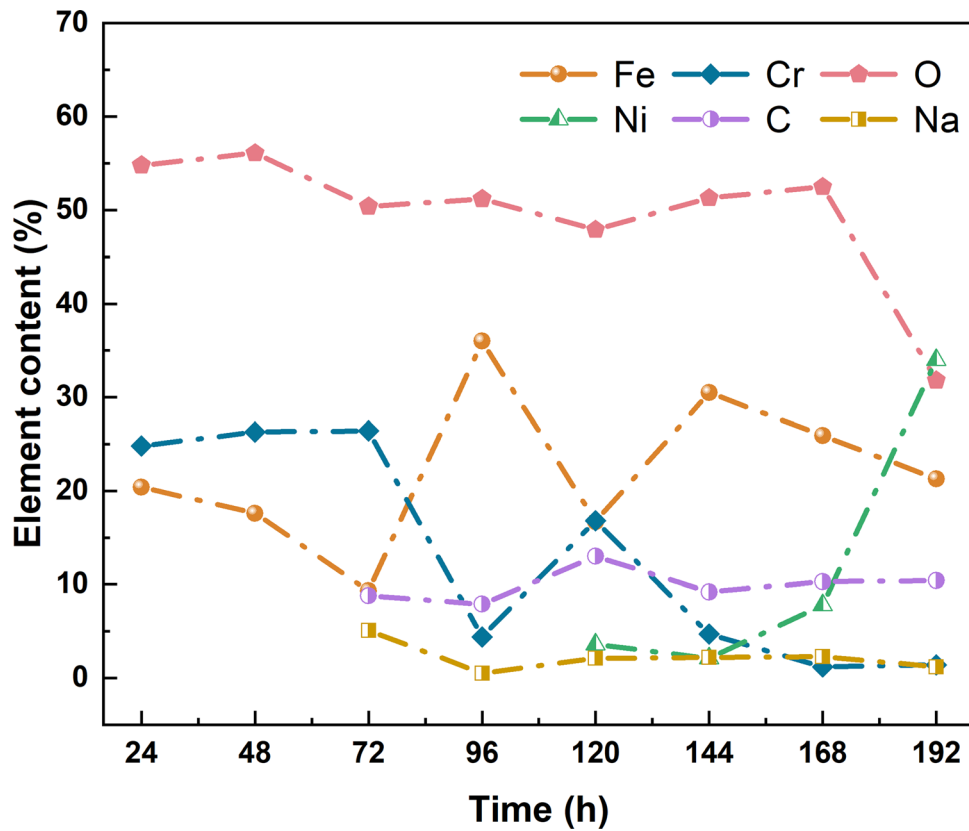


Fig. 12 Element content of 0Cr18Ni9 during hot corrosion as a function of time

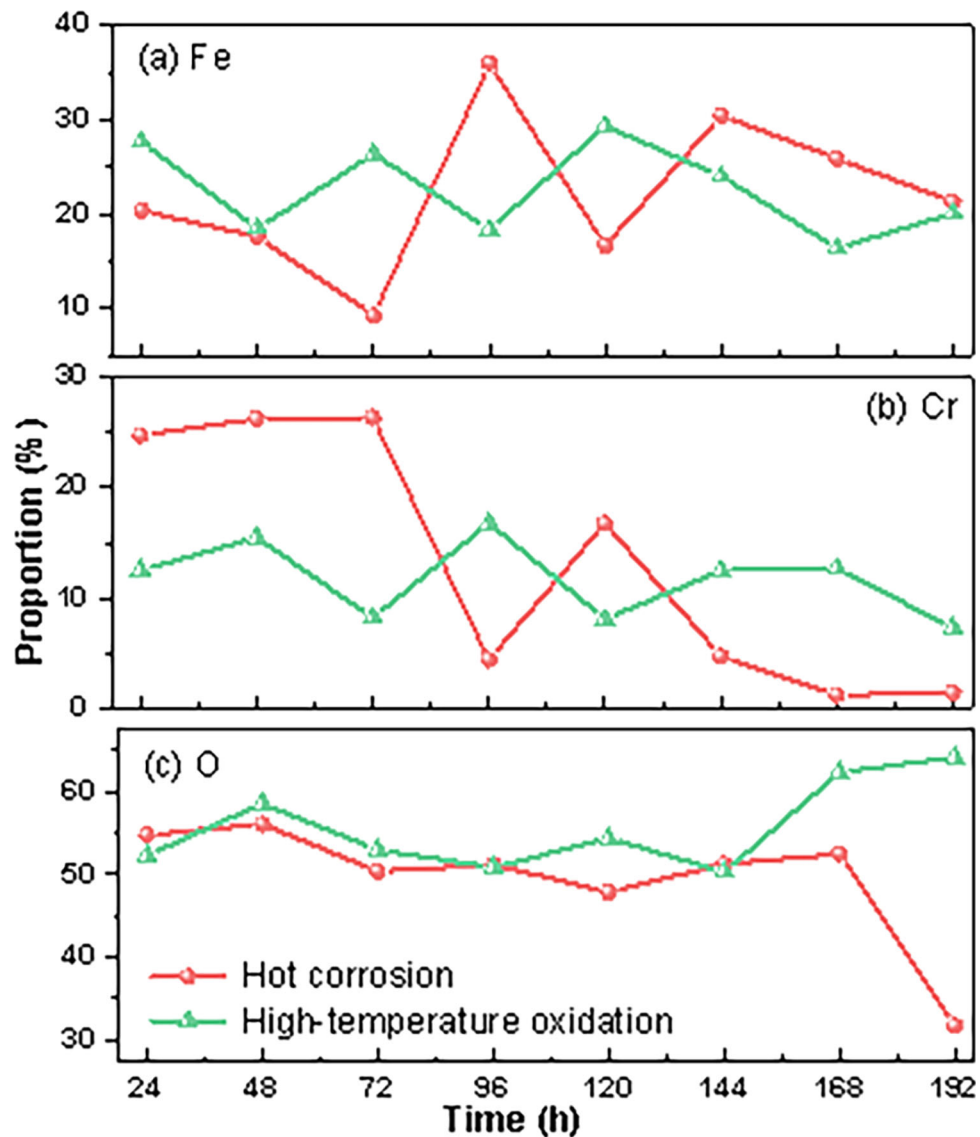


Fig. 13 Content variations of Fe, Cr and O under high-temperature oxidation and hot corrosion of 0Cr18Ni9 as a function of time

possessing the iron-to-oxygen ratios of 0.66, 0.75, and 1, respectively). This discrepancy suggested the presence of other metal elements, such as chromium or nickel, undergoing oxidation processes.

At the beginning of the oxidation reaction, molecular oxygen in the atmosphere was adsorbed onto the surface of the alloy. Subsequently, a rapid chemical reaction occurred between the metal and the adsorbed molecular oxygen (Ref 37). Chromium on the surface of the alloy reacted chemically with molecular oxygen adsorbed on the surface of the alloy to generate chromium oxides, such as Cr_2O_3 . As the reaction proceeded, when the chromium content of the inner layer decreased, iron oxides and chromium oxides underwent an oxidation reaction, and finally spinel particles FeCr_2O_4 (with a ratio of iron to oxygen atoms of 0.25) was generated, which effectively hindered further oxidation of the alloy. The oxidized alloy exhibited a significantly higher carbon content compared to its original state, which remained relatively constant throughout the oxidation process. This was likely due to the adsorption of carbon dioxide from the atmosphere onto the

surface of the alloy. Additionally, the element of nickel was detected at 72 hours and remained constant thereafter, which may be attributed to the fact that nickel diffused slowly to the surface through the grain boundaries.

3.3.2 Hot corrosion. Figure 12 displays the element content of 0Cr18Ni9 during hot corrosion as a function of time. At 72 hours, the element of oxygen and sodium were simultaneously detected on the surface of alloy and the sodium content remained stable at a consistently low level (approximately 1.67%) throughout the corrosion process, which could correspond to sodium carbonate or sodium bicarbonate. Additionally, Fig. 9(d) reveals the circular granular morphology of the holes, which are similar in size to SHOU DPEA. This indicates that SHOU DPEA might enter the alloy through these openings, suggesting a possible interaction between SHOU DPEA and the corrosion process. Within 0-168 hours, the percentage of oxygen content was highest, which may be attributed to the oxidation of the alloy. However, the oxygen level drastically dropped at 192 hours. Simultaneously, the

nickel content notably increased, surpassing the oxygen content for the first time. This may be due to the fact that the porous and loose matrix facilitated the diffusion of alloy elements through the matrix, driven by a concentration gradient. More specifically, the diffusion of nickel atoms from the interior of the grain to the surface of the oxide matrix was enhanced, resulting in the increased nickel content observed on the surface. The higher concentration of nickel on the surface provides beneficial effects for the protective properties of the alloy. Nickel is known to form a passivating oxide layer that can help protect against further oxidation and corrosion. Therefore, the increased transfer of nickel elements to the surface contributes to the enhancement of the alloy's resistance to oxidative degradation (Ref 38). The surface layer of oxides in the central region of the 0Cr18Ni9 alloy was observed to peel off at 192 hours, as shown in Fig. 6(i), which may cause a drop in the oxygen element. Additionally, there was a significant decline in iron and chromium elements during this period, indicating that the shedding surface layer likely consisted of iron or chromium oxides. Interestingly, the initial carbon content of the 0Cr18Ni9 alloy was 0.07%, which was below the detection limit of EDS. Nevertheless, at 72 hours, both carbon and sodium elements were detected simultaneously and carbon content remained relatively stable, with an average content of 9.9%. This finding may be attributed to the presence of sodium carbonate or CO_2 (Ref 39), byproducts resulting from the decomposition of SHOU DPEA. The content of chromium remained essentially steady throughout three corrosion cycles before experiencing a drastic decline at 96 hours, which is consistent with the observation in Fig. 7(e). Generally speaking, chromium content determines the corrosion resistance capability and is a vital factor in assessing the performance of stainless steel (Ref 35). The first significant decrease in chromium content in the 0Cr18Ni9 alloy occurred between 72 and 96 hours, with a decrease rate of 0.92% per hour. Subsequently, a second significant decrease occurred between 120 and 168 hours, with a decline rate of 0.30% per hour. These decreases resulted in the formation of a noticeable Cr-poor layer on the surface of the alloy. The "sensitization temperature zone" for intergranular corrosion of austenitic stainless steel falls between 450 and 850 °C. In the process of aircraft engine operation, as the temperature increased, the risk of chromium carbide formation at grain boundaries of alloy increased in the sensitization temperature zone. The more opportunities for the formation of "chromium-poor zones" at grain boundaries, the higher the likelihood of intergranular corrosion. From Fig. 12, it can be found that nickel was detected at 120 hours, and its content also increased with the corrosion time, suggesting that the nickel inside the alloy diffused to the surface (Ref 40).

3.3.3 Comparison. Further comparative analyses of the three main elements (Fe, Cr, and O) are presented below, considering that the content of Na, Ni, and C elements accounted for a relatively small percentage (The localized elevation of Ni element in the range of 168-192 hours have been explained in the previous section). Figure 13 illustrates the variations in the content of Fe, Cr and O after high-temperature oxidation and hot corrosion of 0Cr18Ni9 as a function of time. It is evident from Fig. 13(a) and (b) that the Fe and Cr elements in 0Cr18Ni9 were significantly different in the two cases. In the oxidation tests of alloys, Fe and Cr variations were more prone to follow periodic regularity. In contrast, in the corrosion tests of alloys, selective dissolution of the substrate occurred, and the

dispersion of Fe and Cr elements was not homogeneous, with considerable variations in content at different times. The content of Cr at 168 hours was only 4.8% of that at 24 hours, which resulted in a significant decrease in corrosion resistance. The trend of O content change tended to be consistent from 0 to 144 hours. At 144 hours, the oxygen content increased significantly. This observation may be attributed to the fact that the substrate became loose under prolonged high-temperature oxidation, which accelerated the diffusion of elemental oxygen. In contrast, under hot corrosion conditions, the elemental content of Fe, Cr, and O decreased at 168 hours, as depicted in Fig. 13(a), (b), and (c). This phenomenon originated from the rupture and shedding of oxides on the alloy surface.

3.4 FTIR Analysis

3.4.1 High-Temperature Oxidation. The FTIR spectra of 0Cr18Ni9 at different oxidation cycles are presented in Fig. 14. In the first oxidation cycle, the spectral curve is essentially the same as that of the blank sample. At 48 hours, two small insignificant peaks appeared in the range of 500-750 cm^{-1} and 750-900 cm^{-1} , which originate from the stretching vibration and bending vibration of Fe-O bonds, respectively. The spectral curves exhibited prominent peaks within the wavelength range of 825-864 cm^{-1} at 72 hours, which may originate from the absorption peaks of FeCr_2O_4 (Ref 41, 42). The absorption peak at 644 cm^{-1} in the case of 168 hours also came from spinel FeCr_2O_4 (Ref 41, 42). Additionally, the absorption peak near 550 cm^{-1} came from the vibration of the iron-oxygen bonding. As the oxidation time increases, oxygen molecules react with iron oxide at high temperatures to form FeCr_2O_4 , a spinel structure oxide. Spinel FeCr_2O_4 has a different structure and chemical bonding, which can result in different vibration frequencies and intensities, leading to a decrease in the intensity of the vibration peak near 550 cm^{-1} . Therefore, the transformation of iron oxide to FeCr_2O_4 during the oxidation process is likely the main reason for the observed variation in the intensity of the vibration peak near 550 cm^{-1} . It was noteworthy that after the normalization process, the peak intensities of the Fe-O and FeCr_2O_4 vibrations in the spectrum display a trend with increasing oxidation time: the Fe-O peak becomes smaller while the FeCr_2O_4 peak becomes larger. It suggested that some iron oxides may be converted into FeCr_2O_4 with the rise of high-temperature oxidation time, which was consistent with the findings in Fig. 13.

3.4.2 Hot corrosion. The spectra of 0Cr18Ni9 at different corrosion cycles are shown in 0. The observed absorption peaks at wavelengths of 2930 cm^{-1} , 1520 cm^{-1} , 3020 cm^{-1} , and 1303 cm^{-1} were derived from the four intrinsic vibrational fundamental frequencies of the methane molecule (Ref 14). These peaks were generated due to the chain breaking of FP. The absorption peaks at wavelengths of 1620 cm^{-1} , 1440 cm^{-1} , and 1070 cm^{-1} were attributed to sodium carbonate, with the absorption peak at 1070 cm^{-1} corresponding to the stretching vibration of the C-O bond, while the absorption peaks at 1620 cm^{-1} and 1440 cm^{-1} were attributed to C-O-Na (Ref 43, 44). Spinel FeCr_2O_4 was the source of absorption bands at wavelengths of 941 cm^{-1} , 822 cm^{-1} , and 708 cm^{-1} (41, 42). The absorption peaks at 3380 cm^{-1} and 545 cm^{-1} were generated by Fe-O bond vibrations, indicating the presence of Iron oxide black, ferric oxide, or ferrous oxide (Ref 42, 45, 46). In particular, the peaks at 3300 cm^{-1} and 3190 cm^{-1} represented

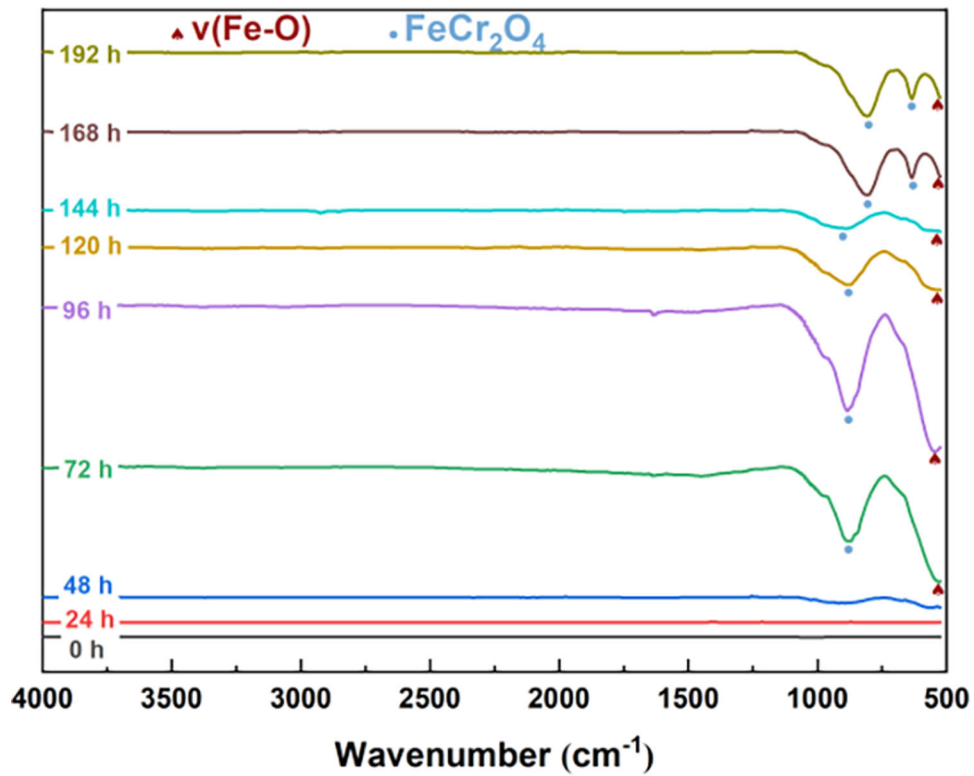


Fig. 14 FTIR spectra of 0Cr18Ni9 at different oxidation cycles. (b) Hot corrosion

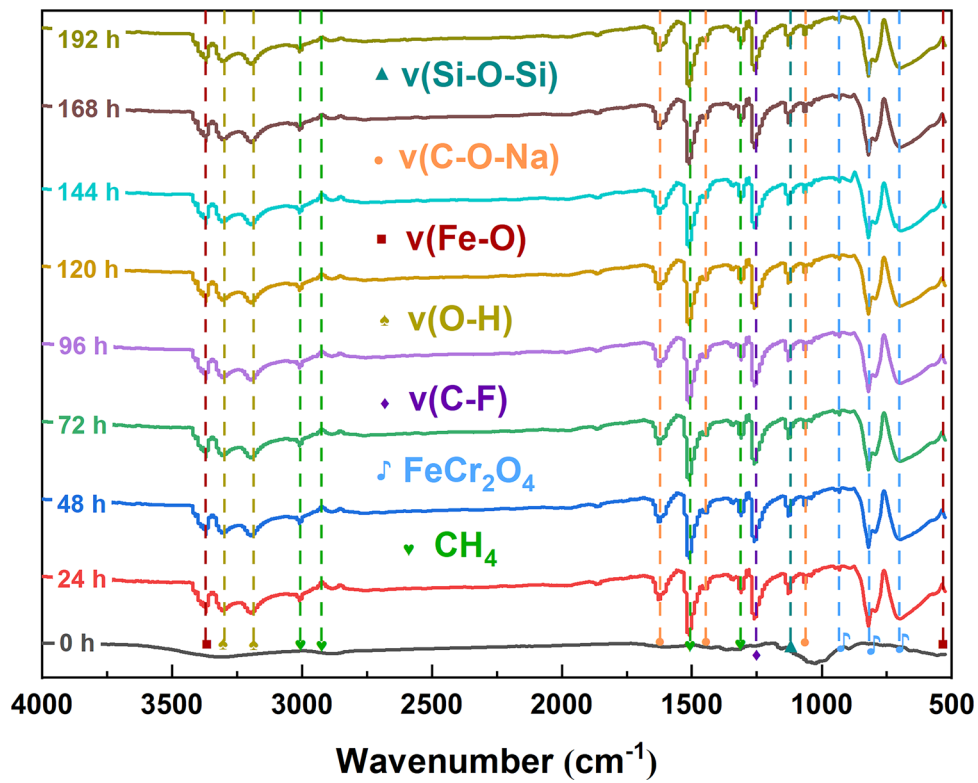


Fig. 15 FTIR spectra of 0Cr18Ni9 at different corrosion cycles

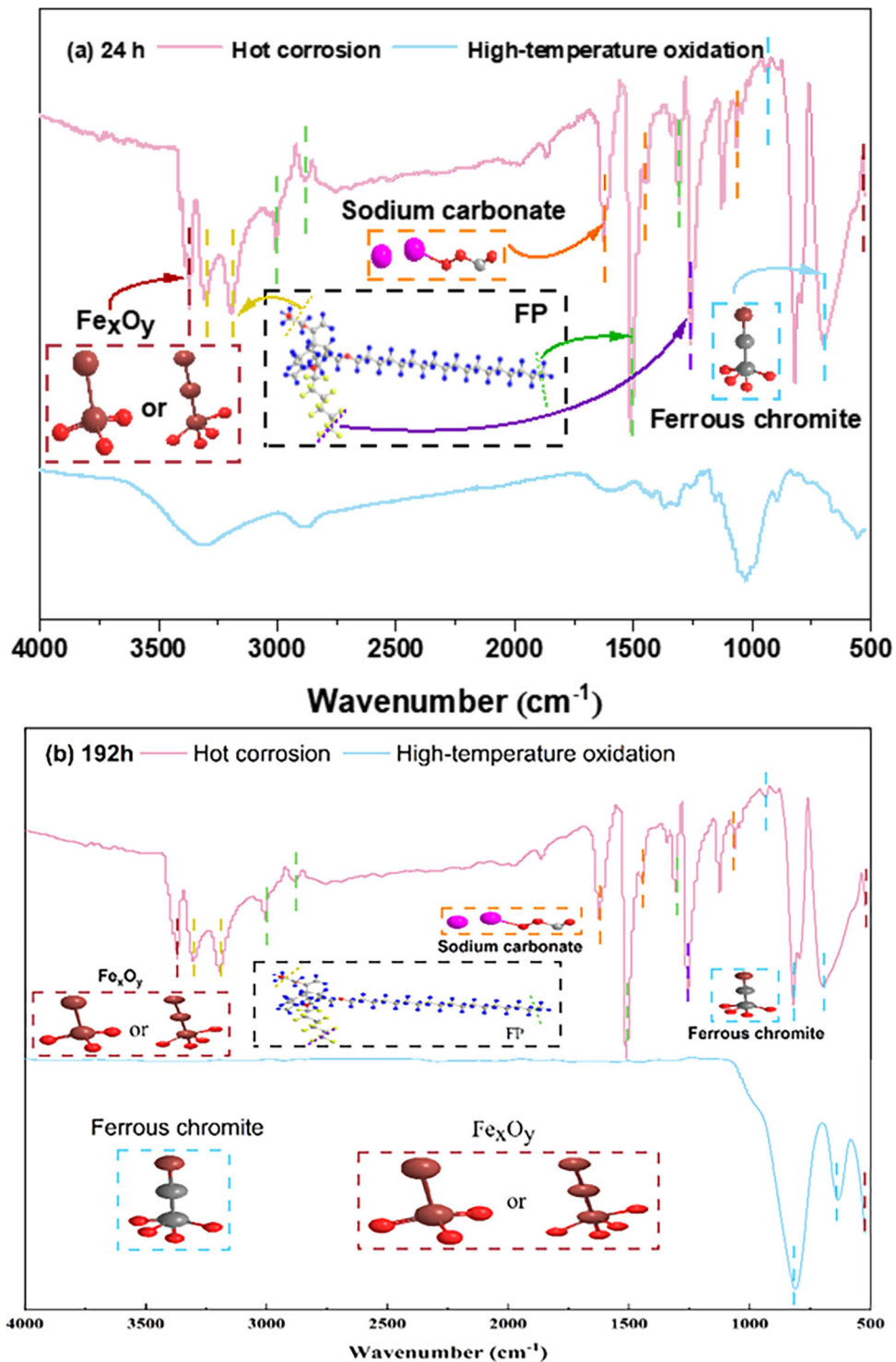


Fig. 16 Comparison of FTIR spectra for hot corrosion and high-temperature oxidation of 0Cr18Ni9 at (a) 24 hours and (b) 192 hours

O-H based peaks, with the absorption peak at 3300 cm^{-1} being a characteristic absorption peak of water (Ref 47, 48) and the O-H bond in the C₆-fluorinated acrylate copolymer potentially accounting for the absorption peak at 3190 cm^{-1} . Remarkably, the absorption peaks at 1130 cm^{-1} and 1260 cm^{-1} represented the Si-O-Si and C-F bonds of the SHOU DPEA, respectively.

3.4.3 Comparison. The infrared spectra for hot corrosion and high-temperature oxidation of 0Cr18Ni9 at 24 hours are depicted in Fig. 16(a). The results show that 0Cr18Ni9 did not undergo significant changes and remained in the austenitic phase for oxidation at 24 hours. Spinel FeCr₂O₄ and iron oxides, which may be Fe₂O₃ and Fe₃O₄, were produced when

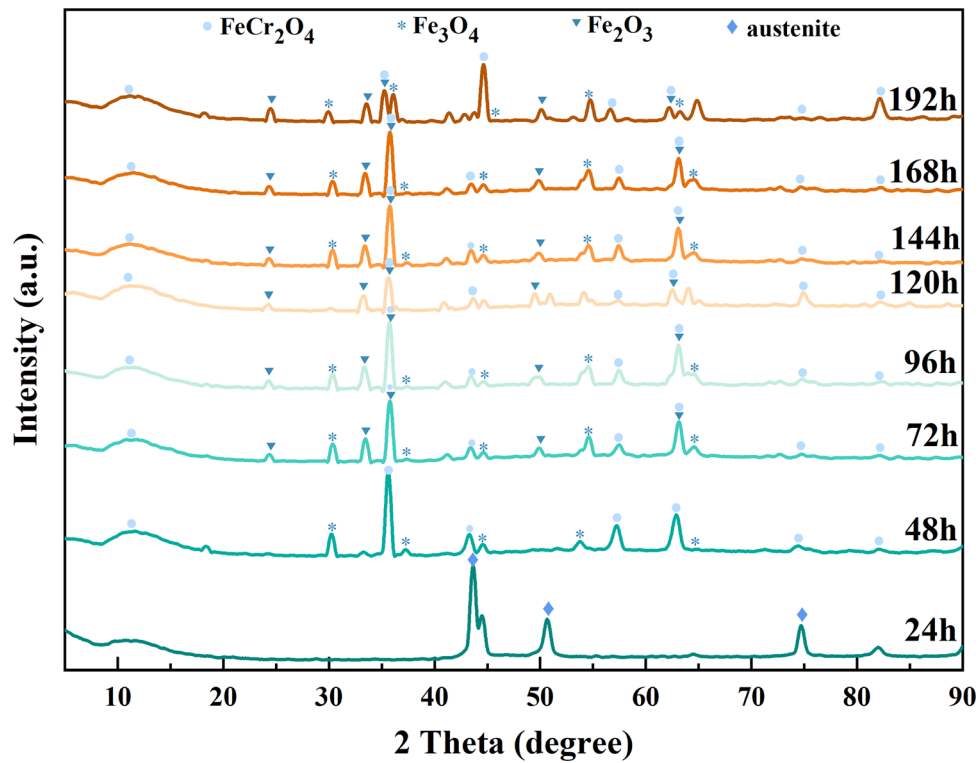


Fig. 17 XRD diffractogram of 0Cr18Ni9 at different high-temperature oxidation cycles

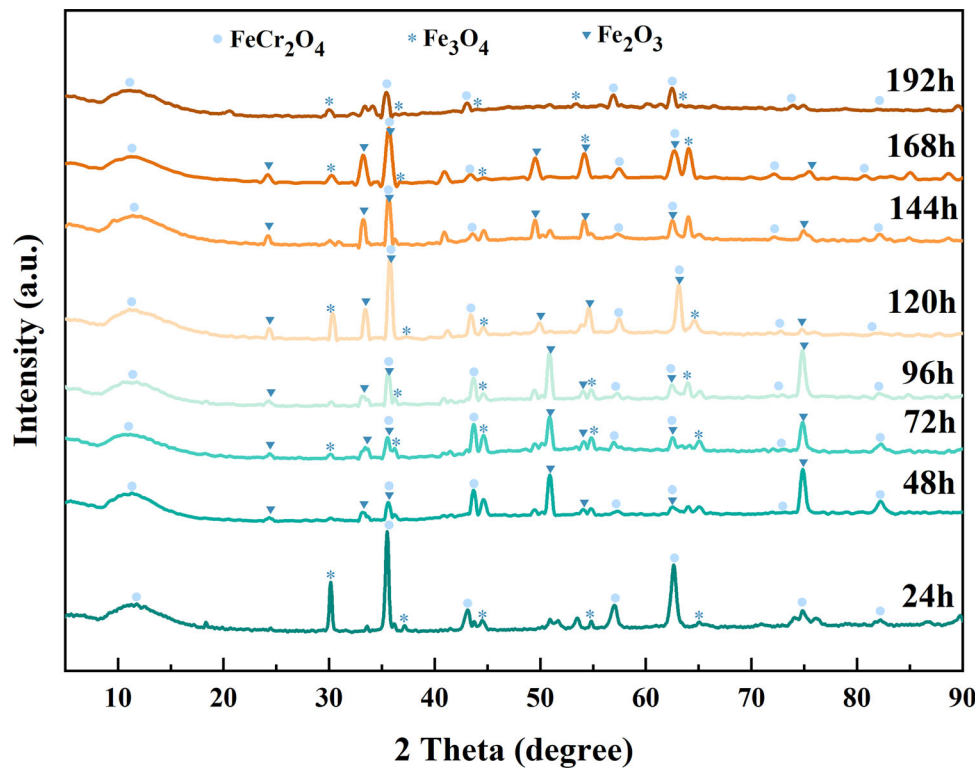


Fig. 18 XRD diffractogram of 0Cr18Ni9 at different hot corrosion cycles

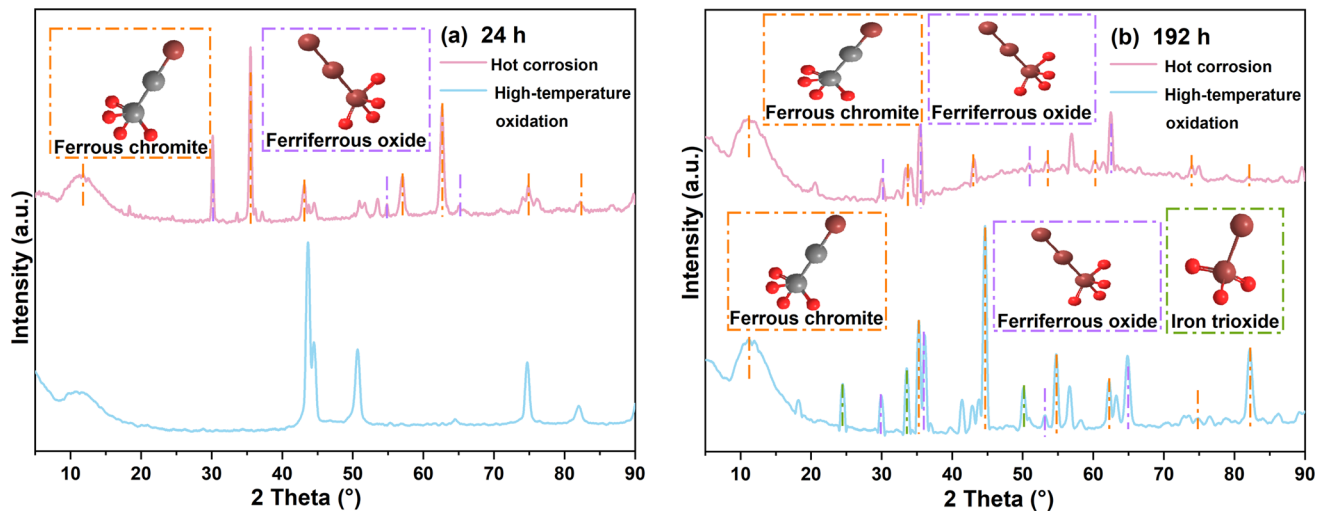


Fig. 19 Comparison of the XRD diffractogram for high-temperature oxidation and hot corrosion of 0Cr18Ni9 at (a) 24 hours and (b) 192 hours

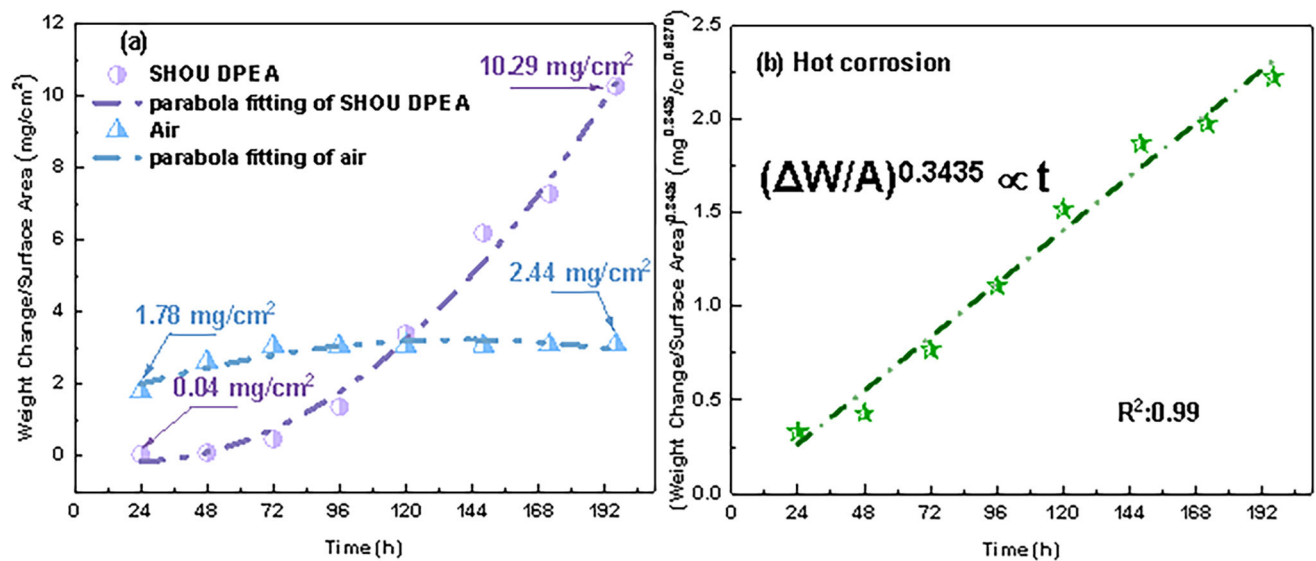


Fig. 20 Oxidation / corrosion kinetic profile of 0Cr18Ni9 as a function of time

corrosion of 0Cr18Ni9 alloy occurred in SHOU DPEA. Notably, regardless of the high-temperature oxidation or hot corrosion by SHOU DPEA, the absorption peaks of Fe-O bonds and FeCr_2O_4 were detected with similar intensities at 192 hours, as illustrated in Fig. 16(b). Thus, it may be concluded that SHOU DPEA does not alter the type of oxidation/corrosion products of 0Cr18Ni9 alloy.

3.5 XRD Analysis

3.5.1 High-Temperature Oxidation. The XRD diffractogram of 0Cr18Ni9 at different high-temperature oxidation cycles is exhibited in Fig. 17. The characteristic austenite diffraction peaks for 0Cr18Ni9 were observed at 24 hours at 43.60° , 50.60° , and 74.60° (Ref 49), which suggested that no significant oxidation of 0Cr18Ni9 had occurred at 24 hours. This finding was consistent with the FTIR data shown in Fig. 14(a). At 48 hours, positions (2θ) of major diffraction peaks were 11.26° , 35.42° , 43.10° , 56.94° , 62.64° , 74.78° , and

82.12° , which were the typical diffraction peaks of FeCr_2O_4 . However, the intensity of these diffraction peaks was weak. At 72 hours, diffraction peaks for FeCr_2O_4 , Fe_3O_4 (30.04° , 37.18° , 44.48° , 54.2° , and 65.02°), and Fe_2O_3 (24.22° , 33.06° , 35.58° , 54.17° , 62.50° , and 74.86°) were observed. The intensity of the diffraction peaks for Fe_2O_3 was higher than that of Fe_3O_4 . Particularly, the positions of the diffraction peaks from 96 hours to 120 hours closely resembled those from 48 hours to 72 hours. After 144 hours, the position of the diffraction peak remained constant, but the intensity of the peak decreased over time. This means that the major oxidation products are Fe_3O_4 , Fe_2O_3 and FeCr_2O_4 . Meanwhile, the oxidation rate of the alloy appeared to slow down.

3.5.2 Hot Corrosion. The XRD diffractogram of 0Cr18Ni9 at different hot corrosion cycles is displayed in Fig. 18. At 24 hours, the positions (2θ) of significant diffraction peaks at 11.26° , 35.42° , 43.10° , 56.94° , 62.64° , 74.78° , and 82.12° were observed. These peak positions were consistent

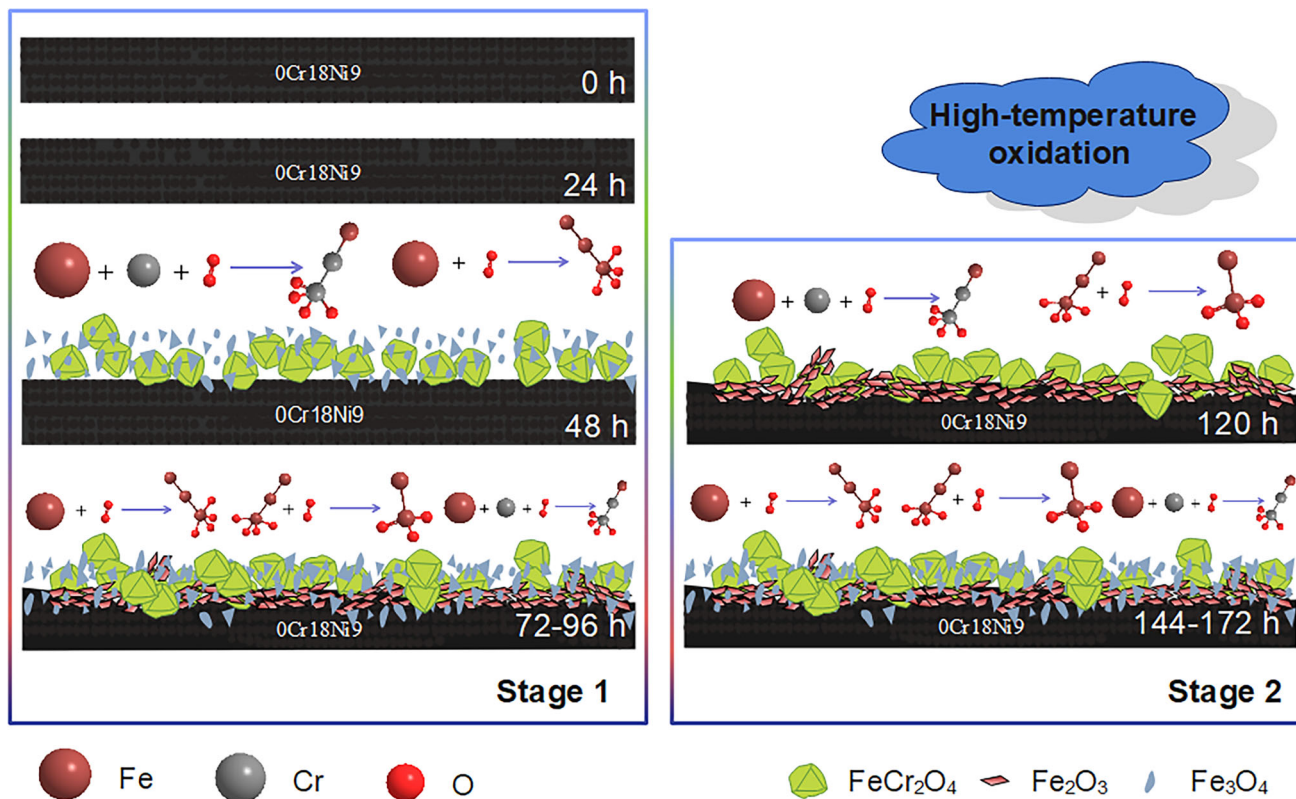


Fig. 21 The chemical reaction mechanism of 0Cr18Ni9 during the high-temperature oxidation process

with the diffraction peaks observed for the alloy oxidized at 24 hours, indicating that FeCr_2O_4 was one type of products in the 24-hour corrosion process. With the progress of corrosion, the positions (2θ) of distinctive Fe_3O_4 diffraction peaks were observed at 30.04° , 37.18° , 44.48° , 54.2° , and 65.02° (Ref 50). Although FeCr_2O_4 was still present, the dense diffraction peaks for Fe_3O_4 disappeared at 48 hours. This occurs because Fe_3O_4 may undergo further reactions with oxygen molecules to form Fe_2O_3 . This transformation process alters the crystal structure of Fe_3O_4 , thereby preventing the generation of prominent diffraction peaks. In contrast, the positions (2θ) of distinctive Fe_2O_3 diffraction peaks (Ref 51) were observed at 24.22° , 33.06° , 35.58° , 54.17° , 62.50° , and 74.86° . It may indicate that the generated Fe_3O_4 can further react with oxygen to form Fe_2O_3 (Ref 52). In the range of 72-120 hours, FeCr_2O_4 , Fe_3O_4 , and Fe_2O_3 were all present simultaneously. Notably, Fe_3O_4 was transformed into Fe_2O_3 at 144 hours. It is worth mentioning that after eight hot corrosion cycles, the predominant corrosion product of 0Cr18Ni9 was FeCr_2O_4 , and the intensity of Fe_3O_4 diffraction peak was significantly reduced at 192 hours.

3.5.3 Comparison. The XRD diffractogram for high-temperature oxidation and hot corrosion of 0Cr18Ni9 at 24 hours are illustrated in Fig. 19(a). The curves demonstrated that after the first cycle, 0Cr18Ni9 remained in the austenite phase in the oxidation tests. However, in the corrosion test, two oxides, namely Fe_3O_4 (magnetite) and FeCr_2O_4 (chromite), were formed on 0Cr18Ni9. At 192 hours, Fe_2O_3 , Fe_3O_4 , and FeCr_2O_4 were identified as oxidation products for the high-temperature oxidation, as illustrated in Fig. 19(b). However, for the hot corrosion case, the corrosion products at 192 hours were Fe_3O_4 and FeCr_2O_4 . After normalization, the intensity of the

diffraction peaks in hot corrosion was greater than that in high-temperature oxidation, suggesting that the addition of the SHOU DPEA might accelerate the oxidation reaction of the 0Cr18Ni9 alloy, producing more FeCr_2O_4 . The XRD analysis was consistent with the findings stated in Sect. 3.4.

3.6 Kinetic Analysis

In this study, the ultimate mass change of 0Cr18Ni9 is caused by the increase in the mass of the oxide. Eq. (4) and (5) in Sect. 2.4 are used to determine the normalized corrosion rate, and the oxidation/corrosion kinetic curves of 0Cr18Ni9 over time are displayed in Fig. 20(a). As can be shown from Fig. 20(a), the cumulative weight gain of 0Cr18Ni9 during high-temperature oxidation at 871°C for 24 hours and 192 hours was 1.78 mg/cm^2 and 2.44 mg/cm^2 , respectively. Initially, the oxidation was primarily governed by chemical reaction (Ref 53), resulting in a large oxidation rate. However, as the oxidation cycle increased, oxygen diffused from the external environment into the interior of 0Cr18Ni9, forming an oxide film on its surface. The oxidation was then controlled by the diffusion of elements within the oxide film (Ref 54, 55). As the thickness of the oxide film increased, the diffusion of oxygen became more and more difficult, resulting in a decrease in the oxidation rate.

The cumulative weight gain of 0Cr18Ni9 during hot corrosion at 871°C for 24 hours and 192 hours in Fig. 20(a) was 0.04 mg/cm^2 and 10.29 mg/cm^2 , respectively. The initial rate of hot corrosion was low, but it significantly increased after 72 hours. This was due to the pyrolysis of SHOU DPEA that covered the surface of 0Cr18Ni9 during the initial stage of corrosion. The generation of carbon dioxide slowed down the

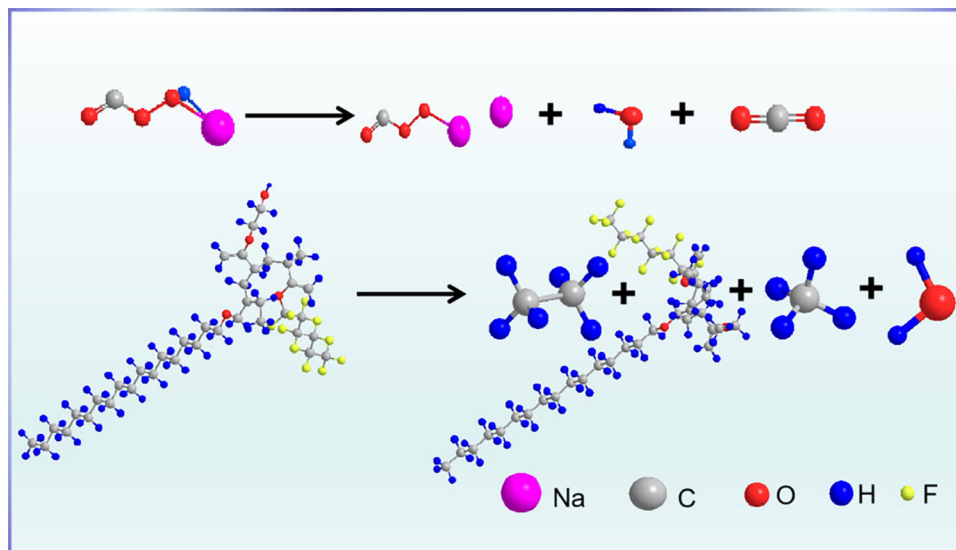


Fig. 22 Thermal decomposition mechanism of SHOU DPEA

interaction between the alloy and oxygen. As the corrosion cycle progressed, the 0Cr18Ni9 alloy generated a large number of voids in the magnetite (antispinel structure) and Fe-Cr oxides (spinel structure) (Both of magnetite and Fe-Cr oxides were corrosion products of the 0Cr18Ni9 alloy), and the corrosion rate of the alloy was determined by the diffusion of metal cations or oxygen anions that were generated through the pyrolysis of the SHOU DPEA. It is worth noting that before 120 hours, the rate of high-temperature oxidation is higher than the rate of hot corrosion. This is due to that the SHOU DPEA covered the surface of the 0Cr18Ni9 alloy and inhibited the oxidation of the alloy. Furthermore, the oxidation rate and the corrosion rate of the alloy are equal at 120 hours. After 120 hours, the oxidation rate of the alloy basically tended to be constant, but the corrosion rate of the alloy grew rapidly, which may be due to that the presence of SHOU DPEA accelerated the oxidation within the alloy.

The oxidation kinetic equations of 0Cr18Ni9 for hot corrosion and high-temperature oxidation at 871 °C are found to follow the parabolic equations $\Delta W/A = -0.01384 - 0.01425t + 3.4302 \times 10^{-4}t^2$ and $\Delta W/A = 1.4376 + 0.02551t - 9.0856 \times 10^{-5}t^2$, respectively. In particular, in hot corrosion tests, the mass weight gain of 0Cr18Ni9 over time follows Wagner's parabolic law, indicating that the corrosion of the metal is governed by the diffusion of positive and negative ions within the oxide film. Fig. 20(b) presents the fitting equation of hot corrosion, $(\Delta W/A)^{0.3435} = -0.02446 + 0.01191t$, $R^2 > 0.99$. As a result, the reaction index (n) and the reaction rate (K_n) of 0Cr18Ni9 in a simulated aircraft engine compartment working environment with SHOU DPEA is 0.3435 and 0.01191 mg²/h, respectively.

3.7 High-Temperature Oxidation / Hot Corrosion Mechanism

Based on the research findings presented in Sect. 3.1 to 3.6, the high-temperature oxidation process of 0Cr18Ni9 can be divided into two stages: a rapid oxidation stage (0-96 hours) and an oxidation equilibrium stage (96-192 hours). Figure 21 depicts the chemical reaction mechanism during the high-temperature oxidation process. In the rapid oxidation stage (0-

96 hours), significant changes of surface morphology are observed, and the elemental contents of Fe, Cr, and O show periodic changes with time. The oxidation rate increases as a function of time. In this stage, the alloy maintains its austenitic structure for the first 24 hours. At 48 hours, the iron and chromium elements react with oxygen to form FeCr₂O₄ and Fe₃O₄, respectively. From 72 to 96 hours, Fe₃O₄ further reacts with oxygen to form Fe₂O₃.

In the oxidation equilibrium stage (96-192 hours), the differences of surface morphology in the alloy substrate decrease with time. At 120 hours, all the Fe₃O₄ converts to Fe₂O₃ upon the reaction with oxygen. During the period of 144-172 hours, the oxidation products remain consistent and consist of FeCr₂O₄, Fe₃O₄, and Fe₂O₃. This indicates that no further changes in the types of oxide compounds occur during this period. Additionally, the presence of these oxides suggests a complex oxidation process involving the formation of FeCr₂O₄ (chromite), Fe₃O₄ (magnetite), and Fe₂O₃ (hematite) on the surface of 0Cr18Ni9 alloy and the uniformly dense oxide layer which forms through the alloy's reaction with oxygen effectively impedes the diffusion of oxygen atoms into alloy, thereby reducing the oxidation rate.

Since the molten salt adhered to the surface of the 0Cr18Ni9 alloy during the hot corrosion process and 80% decomposition of SHOU PEA can be achieved at 70-150 °C (Ref 36), several specific reactions firstly occurred at the interface between the molten salt and metal, including the decomposition of sodium bicarbonate to sodium carbonate, water and carbon dioxide, and decomposition of FP fluorocarbon surfactant, as shown in Fig. 22.

Understanding the detailed mechanisms and factors influencing the hot corrosion is crucial for developing protective measures and materials that can withstand such high-temperature corrosive environments. Note that the essence of the hot corrosion is actually an accelerated oxidation behavior. The hot corrosion process of 0Cr18Ni9 can be divided into two stages: an initial slow incubation stage (0-48 hours) and an accelerated corrosion stage (48-192 hours). The reaction mechanism of hot corrosion of 0Cr18Ni9 at 871 °C is illustrated in Fig. 23. During the initial slow incubation stage (0-48 hours), triangular pits and rose-shaped protrusions are observed on the surface.

Hot corrosion

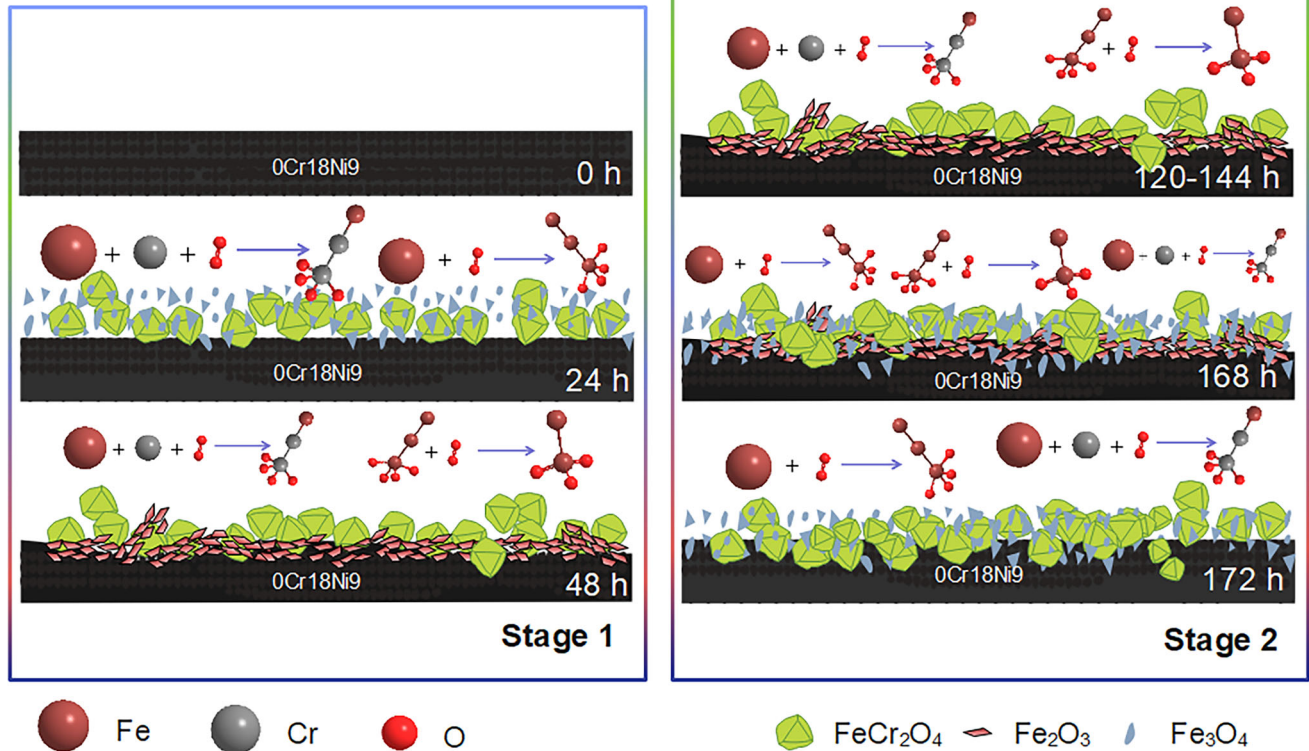


Fig. 23 The chemical reaction mechanism of 0Cr18Ni9 during the hot corrosion process

The elemental contents of Fe, Cr, and O undergo minimal changes over time. At 24 hours, oxygen reacts with chromium and iron from 0Cr18Ni9 to generate FeCr₂O₄ with a spinel structure. Then, the reaction of iron and oxygen produces dense Fe₃O₄. At 48 hours, Fe₃O₄ further reacts with oxygen to form porous and loosely packed Fe₂O₃.

In the accelerated corrosion stage (48-192 hours), a significant amount of oxide scales peels off the alloy surface, resulting in the fluctuating elemental contents of iron, chromium, and oxygen with the increasing time. Additionally, as the corrosion proceeds in depth, the corrosion rate becomes larger, and the corrosion products are predominantly FeCr₂O₄. Besides, in the corrosion products, Fe₃O₄ and Fe₂O₃ are alternately formed. It is worth noting that SHOU DPEA acts as a catalyst throughout the entire hot corrosion process

4. Conclusions

(1) In the case of high-temperature oxidation, when subjected to an increasing heating cycle, diamond-shaped pits can be observed on the surface of the alloy. These pits gradually extend outward and form steps with vary-

ing depths. During the hot corrosion process, the presence of SHOU DPEA contributes to the alloy's surface turning dark yellow. The surface of the alloy exhibits steep cliff slopes in an orderly manner, resembling the natural formation of mountains. This topographical feature may result from the preferential oxidation or erosion of certain regions of the alloy's surface. Additionally, there is an L-shaped segregation phenomenon in the substrate, along with a chromium-poor layer.

- (2) The high-temperature oxidation products of 0Cr18Ni9 primarily consist of FeCr₂O₄, Fe₂O₃, and Fe₃O₄. As the oxidation cycle progresses, Fe₂O₃ is converted into dense Fe₃O₄. The hot corrosion products observed on the 0Cr18Ni9 substrate are consistent with the high-temperature oxidation products. However, the presence of SHOU DPEA promotes the generation of more FeCr₂O₄.
- (3) The high-temperature oxidation kinetics of 0Cr18Ni9 do not strictly follow a parabolic model. Instead, it can be divided into two stages:

- Rapid oxidation stage (0-96 hours): oxidation reactions occur rapidly with a large rate of oxide layer formation.
- Equilibrium oxidation stage (96-172 hours): the oxidation reactions reach an equilibrium state, and the growth rate

of the oxide layer slows down compared with that in the rapid oxidation stage.

- (4) The hot corrosion kinetics of 0Cr18Ni9 can also be divided into two stages:
- Initial slow incubation stage (0-48 hours): the corrosion rate is relatively low, and visible signs of corrosion are minimal.
 - Accelerated corrosion stage (48-172 hours): the corrosion rate significantly increases, leading to more pronounced corrosion phenomena.

Furthermore, for the case of hot corrosion, the 0.3435th power of the mass loss per unit area of 0Cr18Ni9 is proportional to the time, and the reaction index is 0.3435 and the reaction rate is 0.01191 mg²/h.

Acknowledgments

This work was sponsored by Hong Kong Scholars Program (No. XJ2021025), National Natural Science Foundation of China (No. 52276119), the Fundamental Research Funds for the Central Universities (No. 30922010909), China Postdoctoral Science Foundation (No. 2020M680069) and Jiangsu Planned Projects for Postdoctoral Research Funds (No. 2020Z414).

References

1. B.S. LI Si-cheng. Prediction and analysis of hydrofluorocarbons phase-out management plan in China's fire-fighting industry. 2022. pp. 698-700
2. J. Kim, B. Baek, and J. Lee, Numerical Analysis of Flow Characteristics of Fire Extinguishing Agents in Aircraft fire Extinguishing Systems, *J. Mech. Sci. Technol.*, 2009, **23**, p 1877-1884.
3. B. Valeri, T. R. S. R., G. Richard, and N. Marc. Alternative Fire Suppressant Chemicals: A Research Review with Recommendations. Technical Note (NIST TN), National Institute of Standards and Technology, Gaithersburg, MD2001
4. M. Rohilla, A. Saxena, P.K. Dixit, G.K. Mishra, and R. Narang, Aerosol Forming Compositions for Fire Fighting Applications: A Review, *Fire Technol.*, 2019, **55**, p 2515.
5. H.K. Chelliah, P.C. Wanigarathne, A.M. Lentati, R.H. Krauss, and G.S. Fallon, Effect of Sodium Bicarbonate Particle Size on the Extinction Condition of Non-Premixed Counterflow Flames, *Combust. Flame*, 2003, **134**, p 261.
6. H. Min, X. Dayong, Z. Ru, P. Xuhai, and P. Renming, Simulation Research of Superfine Powder Extinguishing Agent Movement, *Procedia Eng.*, 2012, **45**, p 1031-1038.
7. A.E. Finnerty. Fire-Extinguishing Powders. Halon Options Technical Working Conference (1997), 206-215
8. X. Yang. The Research on Discharge Performance of Civil Aircraft Fine Dry Powder Fire Extinguishing System. *Civil Aircraft Design & Res.* (2015), 36-39
9. W. Ting, Q. Kuang, W. Hua, and P. Renming, Experimental Research on the Thermal Decomposition of Pentafluoroethane (HFC-125) Extinguishing Agent with n-heptane/Air Pool Fire in Confined Space, *RSC Adv.*, 2016, **6**, p 113713-113719.
10. J. Jin, R. Pan, R. Chen, X. Xu, and Q. Li. Flow and Diffusion Characteristics of Typical Halon Extinguishing Agent Substitute under Different Release Pressures. *Processes* 2020
11. X.S.L.F. Dexu Du. Efficiency characterization of fire extinguishing compound superfine powder containing Mg(OH)₂. *J. Loss Prevent. Proc.* (2018)
12. J. Zhao, Z. Yin, M. Usman Shahid, H. Xing, X. Cheng, Y. Fu, and S. Lu, Superhydrophobic and Oleophobic Ultra-Fine Dry Chemical Agent with Higher Chemical Activity and longer fire-Protection, *J. Hazard. Mater.*, 2019, **380**, 120625
13. W. Ning, Y. Yang, D. Zhang, and R. Pan, Surface Modification of Sodium Bicarbonate Ultrafine Powder Extinguishing Agent by Environmental Friendly Fluorinated Acrylate Copolymers, *Polym. Degrad. Stabil.*, 2021, **187**, 109558
14. Y. Liu, R. Zhang, H. Jing, D. Yu, R. Pan, and R. Chen, Comparative Study on Pyrolysis Characteristics, Kinetics, Volatile Products and Chemical Reactions of Novel Superhydrophobic and Oleophobic Ultra-Fine and Ordinary Dry Powder Extinguishing Agent, *J. Anal. Appl. Pyrol.*, 2023, **172**, 106034
15. X.B. Zhou, T.Q. Wu, L. Tan, J.H. Deng, C. Li, and W. Qiu, A Study on Corrosion of X80 Steel in a Simulated Tidal Zone, *J. Mater. Res. Technol.*, 2021, **12**, p 2224-2237.
16. W.Y.S.M. Wang Wei, Research on the High Temperature Oxidation Performance of Three Types of 310S Stainless Steels, *Contemp. Chem. Ind.*, 2021, **50**, p 1836-1840.
17. Z.Z.L.J. Fengchan, High Temperature Oxidation Behaviour for Austenitic Stainless Steel, *Forg. Stamp. Technol.*, 2021, **46**, p 214-220.
18. Z.C.Q.Z. Zhou Xiaoquan, Experimental Study on Oxide Scale Growth of 304L Stainless Steel Plate in Furnace, *Hot Work. Technol.*, 2021, **50**, p 151-154.
19. J. Chen, Z. Bai, W. Xue, J. Wu, C. Dong, and K. Xiao, Corrosion Life Prediction Model of 304 Stainless Steel in Qingdao Polluted Marine Atmospheric Environment, *Mater. Protect.*, 2019, **52**(48-55), p 68.
20. I. Saefuloh, N. Kanani, F.G. Ramadhan, Y. Rukmayadi, Y. Yusuf, S. Abdullah, and S. Susilo, The Study of Corrosion Behavior and Hardness of AISI Stainless Steel 304 in Concentration of Chloride Acid Solution and Temperature Variations, *J. Phys. Conf. Ser.*, 2020, **1477**, p 52058.
21. L.X. Zhang, N.M. Lin, J.J. Zou, X.Z. Lin, Z.Q. Liu, S. Yuan, Y. Yu, Z.X. Wang, Q.F. Zeng, W.G. Chen, L.H. Tian, L. Qin, R.Z. Xie, B.Q. Li, Z.H. Wang, B. Tang, and Y.C. Wu, Super-Hydrophobicity and Corrosion Resistance of Laser Surface Textured AISI 304 Stainless Steel Decorated with Hexadecyltrimethoxysilane (HDTMS), *Opt. Laser Technol.*, 2020, **127**, 106146
22. J. He, X. Guo, and Y. Qiao., Oxidation and Hot Corrosion behaviors of Nb-Si Based Ultrahigh Temperature Alloys at 900 °C, *J. Nonferr. Metal Soc.*, 2021, **31**, p 207-221.
23. J. Dai, C. Sun, A. Wang, H. Zhang, S. Li, and H. Zhang, High Temperature Oxidation and Hot Corrosion Behaviors of Ti2AlNb Alloy at 923 K and 1023 K, *Corros. Sci.*, 2021, **184**, 109336
24. S. Ocak-Araz, A. Birden, S.U. Bayca, and O. Bican. Effect of Powder-Pack Boronizing on the Microhardness, Wear, and Corrosion Behaviors of AISI 304L Steel. *J. Mater. Eng. Perform.* (2023)
25. S.W. Sun, L.T. Zhang, X. Liu, W. Jin, Q.C. Jiang, and Q.L. Zhao, Nanoparticle Additions Improve the Corrosion Performance of Ni-Cr-Fe-Based Cast Superalloys, *J. Mater. Eng. Perform.*, 2023, **32**, p 8154-8161.
26. P.L.W.R. Wei, Research on the Computer Numerical Controlled Bending Springback Law of 0Cr18Ni9 Stainless Steel Pipes for Aeroengine External Pipeline, *Aeroengine.*, 2022, **48**, p 185-190.
27. L. Lin, R. Yang, F. He, H. Zhong, S. Zheng, and W. You, Hydro-bending technology on aerospace thin-walled elbow parts, *Forg. Stamp. Technol.*, 2021, **46**, p 63-68.
28. M. Blanco, Ó. Martín, F. Santos, P. Tiedra, F. Daroca, and R. López, Thermography IR Applied to Analyse the Influence of the Deformation Speed in the Forming Process, *Procedia Eng.*, 2013, **63**, p 821-828.
29. G.P.W.A. Simkovich, Effect of SiAlON Additions on the Oxidation Resistance OF Cobalt Based Alloys AT 1000 °C, *React. Solids.*, 1987, **3**, p 301-316.
30. Y. Behnamian, A. Mostafaei, A. Kohandehghan, B.S. Amirkhiz, R. Zahiri, W. Zheng, D. Guzonas, M. Chmielus, W. Chen, and J.L. Luo, A Comparative Study on the Oxidation of Austenitic Alloys 304 and 304-Oxide Dispersion Strengthened Steel in Supercritical Water at 650°C, *J. Supercritical Fluids.*, 2017, **119**, p 245-260.
31. H. Wei, G.C. Hou, X.F. Sun, H.R. Guan, and Z.Q. Hu, Oxidation Behavior of a Cast Polycrystalline Ni-Base Superalloy in Air: At 900 and 1000 °C, *Oxid. Met.*, 2007, **68**, p 149-163.
32. Q. Wang, D. Zhou, M. Yu, L. Shi, X. Li, and Q. Sun, Oxidation and Hot Corrosion Behaviors of Mo-Doped NiMoAlY Alloys at 750 °C, *Corros. Sci.*, 2022, **201**, 110262
33. W. Yu, Y. Li, T. Jiang, Y. Wang, B.S. Zhang, X.L. Li, Z.D. Wang, G.M. Xu, and J.D. Li. Solute inverse segregation behavior in twin roll casting of an Al-Cu alloy. *Scripta Mater.* 213 (2022)

34. F. Ji, Z. Wang, and L. Wu, High Temperature Oxidation and Hot corrosion behaviors of Fe_{6.57}Ni_{11.7}Ti₁Mo_{6.6}Co₁₅ High Entropy Alloy, *Mater. Today Commun.*, 2022, **32**, 104063
35. H. Fei, Y. Haicheng, J. Dessau, and C. Xianghai, Novel formation of Ferrite in Ingot of 0Cr17Ni4Cu4Nb Stainless Steel, *ChemEngineering.*, 2018, **2**, p 13–44.
36. H. Sun and J. Liu, Hot Corrosion of Fe and Ni-Based Alloys in Waste-to-Energy Environment at 850 °C, *Eng. Fail. Anal.*, 2022, **133**, 105964
37. M.C.Y.X. Huiqin, High Temperature Oxidation Behavior of 309SMOD Austenitic Heat-Resistant Stainless Steel, *Heat Treat. Met.*, 2021, **46**, p 24–28.
38. O.V. Mythreyi, B.K. Nagesha, and R. Jayaganthan, Microstructural Evolution & Corrosion Behavior of Laser–Powder–Bed–Fused Inconel 718 Subjected to Surface and Heat Treatments, *J. Market. Res.*, 2022, **19**, p 3201–3215.
39. Z. Liu, X. Gao, L. Du, J. Li, P. Li, C. Yu, R.D.K. Misra and Y. Wang, Comparison of Corrosion Behaviour of Low-alloy Pipeline Steel Exposed to H₂S/CO₂-Saturated Brine and Vapour-Saturated H₂S/CO₂ Environments, *Electrochim. Acta*, 2017, **232**, p 528–541.
40. L. Yang, M.P. Bukhovko, A. Malek, L.W. Li, C.W. Jones, P.K. Agrawal, and R.J. Davis. Steam reforming of ethylene over nickel based spinel oxides. *Appl. Catal. A-Gen.* 603 (2020)
41. A.V. Borhade, V.D. Bobade, D.R. Tope, J.A. Agashe and S.S. Kushare, A Highly Selective and Sensitive H₂S Gas Sensor Based on Novel Nanostructure Core-Shell FeCr₂O₄@ZnO@MgO, *J. Inorg. Organomet.*, 2021, **31**, p 4670–4683.
42. F. Paborji, M. Shafiee Afarani, A. Arabi, and M. Ghahari. Solution Combustion Synthesis of FeCr₂O₄ Powders for Pigment Applications: Effect of Fuel Type. *Int. J. Appl. Ceram. Tec.* (2022)
43. S. Joshi, S. Kalyanasundaram, and V. Balasubramanian, Quantitative Analysis of Sodium Carbonate and Sodium Bicarbonate in Solid Mixtures Using Fourier Transform Infrared Spectroscopy (FT-IR), *Appl. Spectrosc.*, 2013, **67**, p 841–845.
44. X. Zhang, J. Wang, Q. Liu, G. Te, Y. Ban, Y. Wang, N. Li, R. He, Y. Zhang, and K. Zhi, The Effects of Sodium and Alkalinity on the Microcrystalline Structure and the Steam Gasification Performance of Shengli lignite, *J. Anal. Appl. Pyrol.*, 2017, **125**, p 227–233.
45. H. Cui, J. Zhang, J. Lu, Z. Li, and D. Li. Research on Modification of Fe₃O₄ Magnetic Nanoparticles with Two Silane Coupling Agents. *Magnetochemistry* 2023
46. K. Wu, W. Huang, J. Wang, and W. Hung, Infrared Stealth and Microwave Absorption Properties of Reduced Graphene Oxide Functionalized with Fe₃O₄, *Mater. Sci. Eng. B*, 2022, **276**, 115575
47. J. Hu, Y. Song, J. Liu, F. Evrendilek, G. Zhang, M. Ren, W. Xie, and S. Sun, Torrefaction-Assisted Oxy-fuel co-combustion of Textile Dyeing Sludge and Bamboo Residues Toward Enhancing Emission-to-Ash Desulfurization in Full Waste Circularity, *Fuel*, 2022, **318**, 123603
48. N. Zhao, E. Yao, H. Ma, J. Zeng, Z. Yu, T. An, F. Zhao, and X. Yu, Studies on Thermokinetic and Reactive Mechanism of Graphdiyne-Based NC Composite via Multi Isoconversional Methods and Model Reconstruction, *Cellulose*, 2022, **29**, p 4365–4379.
49. X. Xu, S. Liu, Y. Liu, K. Smith and Y. Cui, Corrosion of Stainless Steel Valves in a Reverse Osmosis System: Analysis of Corrosion Products and Metal Loss, *Eng. Fail. Anal.*, 2019, **105**, p 40–51.
50. N. Lotfian, A. Nourbakhsh, S.N. Mirsattari, A. Saberi and K.D. Mackenzie, A Comparison of the Effect of Nanostructured MgCr₂O₄ and FeCr₂O₄ Additions on the Microstructure and Mechanical Properties of Direct-Bonded Magnesia-Chrome Refractories, *Ceram. Int.*, 2020, **46**, p 747–754.
51. J. Sahadevan, R. Sojiya, N. Padmanathan, K. Kulathuraan, M.G. Shalini, P. Sivaprakash, and S. Esakki Muthu, Magnetic Property of Fe₂O₃ and Fe₃O₄ Nanoparticle Prepared by Solvothermal Process, *Mater. Today Proc.*, 2022, **58**, p 895–897.
52. I. Chamritski and G. Burns, Infrared-and Raman-Active Phonons of Magnetite, Maghemite, and Hematite: A Computer Simulation and Spectroscopic Study, *J. Phys. Chem. B*, 2005, **109**, p 4965–4968.
53. H. Ebrahimifar and M. Zandrahimi, Mn Coating on AISI 430 Ferritic Stainless Steel by Pack Cementation Method for SOFC Interconnect Applications, *Solid State Ionics*, 2011, **183**, p 71–79.
54. V. Basabe and J. Szpunar, Growth Rate and Phase Composition of Oxide Scales During Hot Rolling Of Low Carbon Steels, *Isij Int. ISIJ INT.*, 2004, **44**, p 1554–1559.
55. S.P. Sah, Corrosion of 304 Stainless Steel in Carbonates melt—A State of Enhanced Dissolution of Corrosion Products, *Corros. Sci.*, 2020, **169**, 108535

Publisher's Note Springer Nature remains neutral with regard to jurisdictional claims in published maps and institutional affiliations.

Springer Nature or its licensor (e.g. a society or other partner) holds exclusive rights to this article under a publishing agreement with the author(s) or other rightsholder(s); author self-archiving of the accepted manuscript version of this article is solely governed by the terms of such publishing agreement and applicable law.